Evaluating the Fairness of Deep Learning Uncertainty Estimates in Medical Image Analysis

Author name(s) withheld EMAIL(S) WITHHELD
Address withheld

Editors: Under Review for MIDL 2023

Abstract

Although deep learning (DL) models have shown great success in many medical image analysis tasks, deployment of the resulting models into real clinical contexts requires: (1) that they exhibit robustness and fairness across different sub-populations, and (2) that the confidence in DL model predictions be accurately expressed in the form of uncertainties. Unfortunately, recent studies have indeed shown significant biases in DL models across demographic subgroups (e.g., race, sex, age) in the context of medical image analysis, indicating a lack of fairness in the models. Although several methods have been proposed in the ML literature to mitigate a lack of fairness in DL models, they focus entirely on the absolute performance between groups without considering their effect on uncertainty estimation. In this work, we present the first exploration of the effect of popular fairness models on overcoming biases across subgroups in medical image analysis in terms of bottom-line performance, and their effects on uncertainty quantification. We perform extensive experiments on three different clinically relevant tasks: (i) skin lesion classification, (ii) brain tumour segmentation, and (iii) Alzheimer's disease clinical score regression. Our results indicate that popular ML methods, such as data-balancing and distributionally robust optimization, succeed in mitigating fairness issues in terms of the model performances for some of the tasks. However, this can come at the cost of poor uncertainty estimates associated with the model predictions. This tradeoff must be mitigated if fairness models are to be adopted in medical image analysis.

Keywords: Uncertainty, Fairness, Classification, Segmentation, Regression, Brain Tumour, Skin Lesion, Alzheimer's Disease

1. Introduction

Deep Learning (DL) models have shown great potential in many clinically relevant applications (e.g. diabetic retinopathy (DR) diagnosis (Gulshan et al., 2016)). Deployment of the resulting models into real-world clinical contexts, and in particular maintaining clinicians' trust, requires that robustness and fairness across different sub-populations are maintained[1]. Unfortunately, several studies have indeed exposed significant biases in DL models across sub-populations (e.g. according to race, sex, age) in the context of medical image analysis (Zong et al., 2022). For example, in Larrazabal et al. (2020), it is shown that a Computer-Assisted Diagnosis system trained on a predominantly male dataset for diagnosing thoracic diseases gives lower performance when tested on female patient images (here, the underrepresented sex). In Burlina et al. (2021), the authors show how data imbalance

1. Ricci Lara et al. (2022) provides a really good overview of the necessity to address the issue of fairness, potential sources of biases, and the remaining challenges, for machine learning models in medical imaging.

© 2023 Anonymous.

in the training dataset leads to a disparity in accuracies across sub-populations (dark vs. light skinned individuals) in the diagnosis of DR. Similar issue of racial bias for groups under-represented in the training data is reported for various medical image analysis tasks such as X-ray pathology classification (Seyyed-Kalantari et al., 2021), cardiac MR image segmentation (Puyol-Antón et al., 2021), and brain MR segmentation (Ioannou et al., 2022).

Several methods have been proposed in the machine learning literature to mitigate the lack of fairness (Mehrabi et al., 2021) in the models. This includes data balancing (Japkowicz and Stephen, 2002; Idrissi et al., 2022), which was shown to be successful for some medical imaging contexts (Puyol-Antón et al., 2021; Ioannou et al., 2022). However, methods to mitigate fairness focus on correcting performance differences across subgroups without considering their effect on the uncertainties associated with the model output. In medical image analysis, however, it has been shown that real clinical contexts would benefit from knowledge about the confidence in the model predictions, when made explicit in the form of uncertainties (Band et al., 2021). Specifically, trust would be established should uncertainties associated with the predictions be higher when the model is incorrect, and low where model outputs are correct. Various successful frameworks for quantifying models uncertainties in the context of medical image analysis have been presented for tasks such as image segmentation (Nair et al., 2020; Jungo and Reyes, 2019), image synthesis (Tanno et al., 2021; Mehta and Arbel, 2018), and image classification (Molle et al., 2019; Ghesu et al., 2019). However, these methods only analyze the output uncertainties for the entire population, without consideration of the results for population subgroups.

In this work, we conjecture that uncertainty quantification can help mitigate some potential risks in clinical deployment related to a lack of robustness and fairness for under-represented populations. However, the uncertainties will only help clinicians make more informed decisions if they are accurate. Specifically, a machine learning model that under-performs for an under-represented subgroup should indicate high uncertainties associated with its output for that subgroup. Conversely, a machine learning model that achieves fairness in terms of performance across different subgroups, but produces low uncertainties for predictions where it makes mistakes, would become less trustworthy to clinicians.

In this paper, we present the first analysis of the effect of popular fairness models at overcoming biases of DL models across subgroups for various medical image analysis tasks, and investigate and quantify their effects on the estimated output uncertainties. Specifically, we perform extensive experiments on three different clinically relevant tasks: (i) multi-class skin lesion classification (Codella et al., 2019), (ii) multi-class brain tumour segmentation (Bakas et al., 2018), and (iii) Alzheimer's disease clinical score (Jack Jr et al., 2008) regression. Our results indicate a lack of fairness in model performance for under-represented groups. The uncertainties associated with the outputs behave differently across different groups. We show that popular methods designed to mitigate the lack of fairness, specifically data balancing (Puyol-Antón et al., 2021; Ioannou et al., 2022; Idrissi et al., 2022; Zong et al., 2022) and robust optimization (Sagawa et al., 2019; Zong et al., 2022) do indeed improve fairness for some tasks. However, this comes at the expense of poor performance of the estimated uncertainties in some cases. This tradeoff must be mitigated if fairness models are to be adopted in medical image analysis.

2. Methodology: Fairness in Uncertainty Estimation

This paper aims to evaluate the effectiveness of various popular machine learning fairness models at mitigating biases across subgroups in various medical image analysis contexts in terms of (a) the absolute performance of the models and (b) the uncertainty estimates across the subgroups. Although general, the framework and associated notations focus on binary sensitive attributes (e.g., sex, binarized ages, disease stages).

Consider a dataset $D = \{X, Y, A\} = \{(x_i, y_i, a_i)\}_{i=1}^{N}$ with N total samples. Here, $x_i \in \mathbb{R}^{P\times Q}$ or $x_i \in \mathbb{R}^{P\times Q\times S}$ represents 2D or 3D input image, y_i represents corresponding ground truth labels, and $a_i = \{0, 1\}$ represents the sensitive binary group-attribute. y_i depends on the task at hand: $y_i \in \{0, 1, .., C\}$ for image-level classification, $y_i \in \mathbb{R}$ for image-level regression, and $y_i \in \{0, 1, ..C\}^{P\times Q}$ or $y_i \in \{0, 1, ..C\}^{P\times Q\times S}$ for 2D/3D voxel-level segmentation. The dataset can be further divided into subgroups, $A = \{0, 1\}$, based on the value of the sensitive attribute: (i) $D^0 = \{X^0, Y^0, A = 0\} = \{(x_i^0, y_i^0, a_i = 0)\}_{i=1}^{M}$ and (ii) $D^1 = \{X^1, Y^1, A = 1\} = \{(x_i^1, y_i^1, a_i = 0)\}_{i=1}^{L}$, where $M + L = N$.

Let us consider a deep learning model $f(., \theta)$ that produces a set of outputs $\hat{Y} = f(X, \theta)$ for a set of input images, X. Although various fairness evaluation measures exist (Hinnefeld et al., 2018), here the *fairness gap* (FG) of a deep learning model is defined as the differences in the task-specific evaluation metric (EM) values between $\hat{Y}$ and Y when conditioned on the sensitive attribute A:

$$\mathrm{FG}(A = 0, A = 1) = |\mathrm{EM}(Y^0, \hat{Y}^0) - \mathrm{EM}(Y^1, \hat{Y}^1)|. \tag{1}$$

A machine learning model is fair for the sensitive attribute A if $\mathrm{FG}(A = 0, A = 1) = 0$. EM differs depending on the task at hand, for example accuracy for image classification, Dice value for segmentation, and mean squared error for image-level regression. EM is calculated for each image separately and then averaged across the dataset for a voxel-level segmentation task. For image classification or regression tasks, EM is calculated directly at a dataset level.

In this work, we focus on Bayesian deep learning (BDL) models (Neal, 2012; Gal and Ghahramani, 2016; Lakshminarayanan et al., 2017; Smith and Gal, 2018), which are widely adopted within the medical image analysis community given their ability to produce uncertainty estimates, $\hat{u}_i$, associated with the model output $\hat{y}_i$. Popular uncertainty estimates include sample variance, predicted variance, entropy, and mutual information (Kendall and Gal, 2017; Gal et al., 2017). Uncertainties $\hat{u}_i$ are typically normalized between 0 (low uncertainty) and 100 (high uncertainty) across the dataset. In the medical image analysis literature, the quality of the estimated uncertainties is evaluated based on the objective of being correct when confident and highly uncertain when incorrect (Mehta et al., 2022; Nair et al., 2020; Lakshminarayanan et al., 2017). To this end, all predictions whose output uncertainties ($\hat{u}_i$) are above a threshold (τ) are filtered (labeled as uncertain). The EM is calculated on the remaining certain predictions ($\hat{Y}_\tau$ and Y_τ) (below the threshold):

$$\mathrm{FG}_\tau(A = 0, A = 1) = |\mathrm{EM}_\tau(Y_\tau^0, \hat{Y}_\tau^0) - \mathrm{EM}_\tau(Y_\tau^1, \hat{Y}_\tau^1)|. \tag{2}$$

At $\tau = 100$, equations 1 and 2 become equivalent. A higher degree of fairness in uncertainty estimation is established through a reduced fairness gap ($\mathrm{FG}_{\tau 1} \leq \mathrm{FG}_{\tau 2}$) when the number of filtered uncertain predictions increases. In other words, when the uncertainty

threshold is reduced ($\tau 1 < \tau 2$), thereby increasing the number of filtered uncertain predictions, the differences in the performances on the remaining confident predictions across the subgroups should be reduced. However, this decrease should not lead to a reduction in overall performance. In other words, it is desirable that $EM_{\tau 1} \geq EM_{\tau 2}$. Conversely, an increase in the fairness gap ($\text{FG}_{\tau 1} > \text{FG}_{\tau 2}$) indicates the undesirable effect of having a higher degree of confidence in incorrect predictions for one of the subgroups.

3. Experiments and Results [2]

Extensive experimentation involves comparisons of two established fairness models against a baseline: (i) A **Baseline-Model**: trained on a dataset without consideration of any subgroup information; (ii) A **Balanced-Model**: trained on a dataset where each subgroup is made to contain an equal number of samples during the training, an established baseline fairness model that focuses on mitigating biases due to data imbalance (Puyol-Antón et al., 2021; Ioannou et al., 2022; Idrissi et al., 2022; Zong et al., 2022); (iii) A **GroupDRO-Model**: trained with GroupDRO loss (Sagawa et al., 2019) to re-weigh the loss for each subgroup, thereby mitigating lack of fairness through the optimization procedure. The number of images in the test set is the same across all subgroups for fair comparisons.

3.1. Multi-class skin lesion classification

Skin cancer is the most prevalent type of cancer in the United States (Guy Jr et al., 2015), which can be diagnosed by classifying skin lesions into different classes.

Dataset: We use the publicly available International Skin Imaging Collaboration (ISIC) 2019 dataset (Codella et al., 2019) for multi-class skin lesion classification. A dataset of 24947 dermoscopic images is provided, with 8 associated disease scale labels, and with high class imbalance. Demographic patient information (e.g. age, gender) is also provided. We consider age as the sensitive attribute (a_i). The entire dataset is divided into two subsets: patient images with age ≥ 60 in subgroup D^0 with a total of 10805 images, and patients with age < 60 in subgroup D^1 with a total of 14045 images. The **Baseline-Model** and the **GroupDRO-Model** are trained on a training dataset where subgroup D^0 contains 8260 images, while subgroup D^1 contains 10892 images. While it appears that subgroup D^1 contains approximately 32% more images, it is not strictly the case for all eight classes. A **Balanced-Model** is trained on a training dataset where both subgroup D^0 and subgroup D^1 contain 7251 images. Both subgroups are balanced for each of the eight classes of the dataset (but not the same across the eight classes).

Implementation Details: An ImageNet pre-trained ResNet-18 (He et al., 2016) model is trained on this dataset. The evaluation metrics (EM) are overall accuracy, overall macro-averaged AUC-ROC, and class-level accuracy. The predictions' uncertainty is measured through the entropy of an Ensemble Dropout model (Smith and Gal, 2018).

Results: For the **Baseline-Model**, all four plots in Figure-1(a) show a high fairness gap between the two subgroups when fewer predictions are filtered based on uncertainties (left

2. Detailed information about the training procedure, class-level distributions of images for different subgroups, and training/validation/testing folds for all three tasks are given in the appendix.

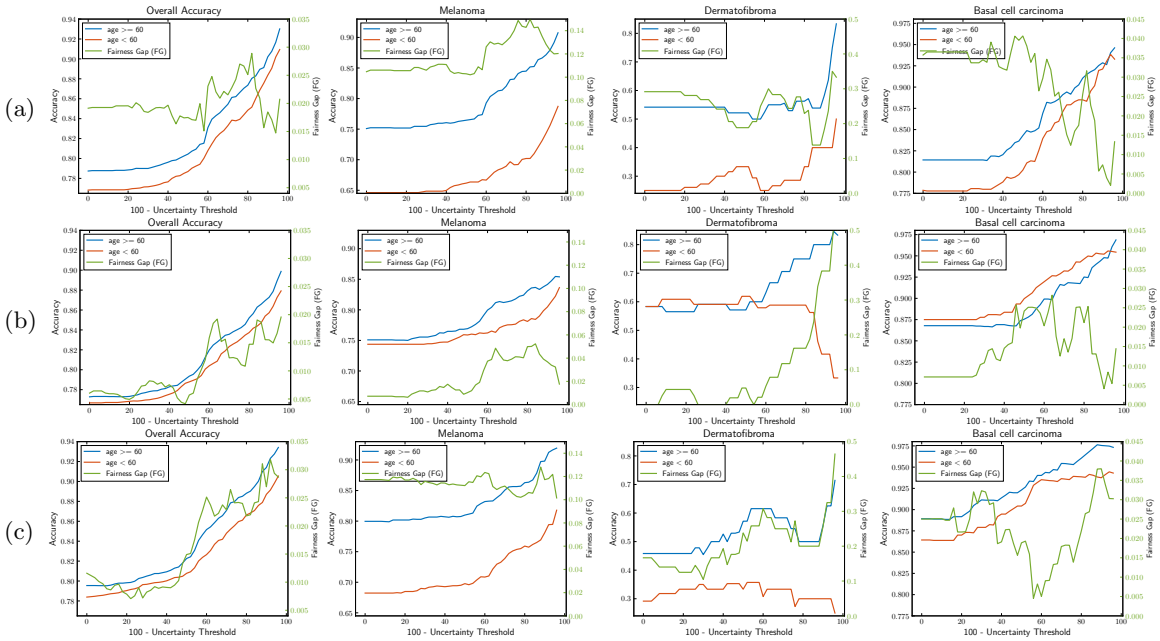

Figure 1: Overall and class-level accuracy (for three classes) against (100 - uncertainty threshold) for (a) **Baseline-Model**, (b) **Balanced-Model**, and (c) **GroupDRO-Model** on the ISIC dataset. Results are shown overall and for each subgroup (D^0: age $>= 60$, D^1: age < 60). For Fairness Gap (FG) refer axis labels on the right.

side of the graph). When filtering more predictions (moving towards the right side of the curve), an increase in the accuracy for each subgroup and a reduction in the fairness gap can be observed. This demonstrates that the model might be incorrect for more images in one of the subgroups, but it usually has *higher uncertainty* in those predictions compared to the other subgroup. Overall Accuracy (Column 1) in Figure-1(b) shows that compared to the **Baseline-Model**, the **Balanced-Model** produces a reduced fairness gap between two subgroups at a low number of filtered predictions (left side of the graph), but at the cost of reduced overall accuracy for each subgroup. The overall accuracy for each subgroup increases with higher uncertainty filtering (towards the right side of the graph). Still, it comes at the expense of a *higher fairness gap*. For classes with a lower number of total images, such as Dermatofibroma in Column 3, filtering out more predictions decreases overall performance for one of the subgroups. This shows that while data balancing could enable better fair models at absolute prediction performance level, it comes at the cost of poor uncertainty estimates. Figure-1(c) shows that the **GroupDRO-Model** gives better overall accuracy and better class-wise accuracy compared to the **Baseline-Model** for classes with a high number of total samples (e.g., Melanoma - Column 2, Basal cell carcinoma - Column 4). But it also shows a high fairness gap when a low number of predictions are filtered (left side of the graph). The fairness gap reduces by filtering more predictions. However, it is not completely mitigated for all of the classes. Overall accuracy and classwise-accuracy for classes with a lower number of samples (ex. Dermatofibroma in Column 3) see a marginal increase in the fairness gap with uncertainty-based filtering. Results indi-

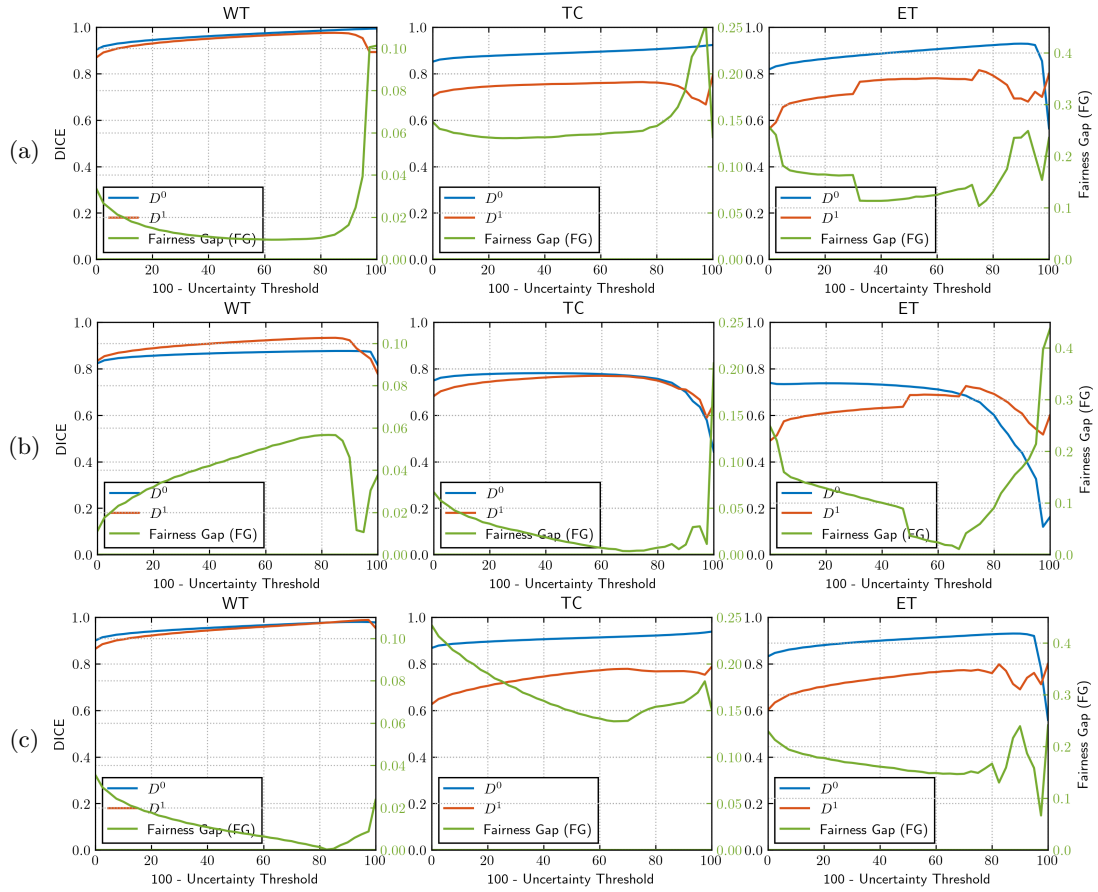

Figure 2: Averaged sample Dice as a function of (100 - uncertainty threshold) for (a) **Baseline-Model**, (b) **Balanced-Model**, and (c) **GroupDRO-Model** on the BraTS dataset. Dice results for whole tumour (WT), tumour core (TC), and enhancing tumour (ET), for both the D^0 and D^1, set are shown in each column. For Fairness Gap (FG) refer axis labels on the right.

cate that the **GroupDRO-Model** might give marginally better absolute performance than the **Baseline-Model**, but it does not produce fair uncertainty estimates across subgroups. Similarly, it can be concluded that different models do not behave consistently across different classes, both in terms of fairness gap and uncertainty evaluation. It indicates that a single model cannot reduce fairness gap and also provide good uncertainty estimation. More results for all eight classes and three models are given in the appendix-A.

3.2. Brain Tumour Segmentation

Automatic segmentation of brain tumours can assist in better and faster diagnosis procedures and surgical planning.

Dataset: We use the 260 High-Grade Glioma (HGG) images from the publicly available Brain Tumour Segmentation (BraTS) 2019 challenge dataset (Bakas et al., 2018). The

image dataset is divided into two subsets based on the volume of the enhancing tumour: 206 images with volumes $> 7000\text{ml}^3$ in subgroup D^0 and 54 images with volumes $\leq 7000\text{ml}^3$ in subgroup D^1. A **Baseline-Model** and a **GroupDRO-Model** are trained on a dataset of 168 samples from D^0 and 30 samples from D^1. While a **Balanced-Model** is trained on a balanced training set with 30 samples from each subgroup.

Implementation Details: A 3D U-Net (Çiçek et al., 2016; Nair et al., 2020) is trained for tumour segmentation. Following the BraTS dataset convention, tumour segmentation performance is evaluated by calculating Dice scores for three different tumour sub-types: enhancing tumor, whole tumor, and tumour core. The predictions' uncertainty is measured through the entropy of an Ensemble Dropout model (Smith and Gal, 2018).

Results: Figure 2 shows that both the **Baseline-Model** and the **GroupDRO-Model** perform similarly for whole tumour (WT) across both subgroups, as an increase in Dice and decrease in the fairness gap is observed with filtering of more voxels in the images (going from left to right in the graph). For the **Balanced-Model** though initially (left most at an uncertainty threshold of 100) the fairness gap is lower compared to the other two models, it increases with the filtering of more voxels in the images. Tumour core (TC) and enhancing tumour (ET) follow a similar trend, where both the **Baseline-Model** and the **GroupDRO-Model** perform similarly. Although for both TC and ET, the **Balanced-Model** doesn't show an increase in the fairness gap between the two subgroups with a decrease in uncertainty threshold (moving from left to right), a decrease in overall performance for both subgroups is observed. This shows that mitigating the fairness gap by filtering out more voxels is insufficient and may lead to a drop in performance in both subgroups. It can be concluded that for a challenging dataset like brain tumour segmentation, the **Balanced-Model** or the **GroupDRO-Model** do not produce fair uncertainty estimates across different subgroups.

3.3. Alzheimer's Disease Clinical Score Regression

Alzheimer's disease (AD) is the most common neurodegenerative disorder in elderly people (Goedert and Spillantini, 2006). For AD, clinicians treat symptoms based on structured clinical assessments (e.g., Alzheimer's Disease Assessment Scale – ADAS-13 (Rosen et al., 1984), Mini-Mental State Examination – MMSE (Folstein et al., 1975)).

Dataset: Experiments are based on the MRIs of a subset (865 patients) of the Alzheimer's Disease Neuroimaging Initiative (ADNI) dataset (Jack Jr et al., 2008) at different stages of diagnosis: Alzheimer's Disease (145), Mild Cognitive Impairment (498), and Cognitive Normal (222). The dataset also provides demographic patient information such as age and gender. Here, we consider age as a sensitive attribute (a_i), divided such that patients with age < 70 are grouped into D^0 (259 patient images), and patients with age ≥ 70 are grouped into D^1 (606 patient images). A **Baseline-Model** and a **GroupDRO-Model** are trained on a dataset that contains 163 samples from D^0 and 440 samples from D^1. While a **Balanced-Model** is trained on a balanced training set with 163 samples from each subgroup.

Implementation Details: A multi-task 3D ResNet-18 model (Hara et al., 2018) is trained on this dataset to regress ADAS-13 and MMSE scores. Root Mean Squared Error (RMSE)

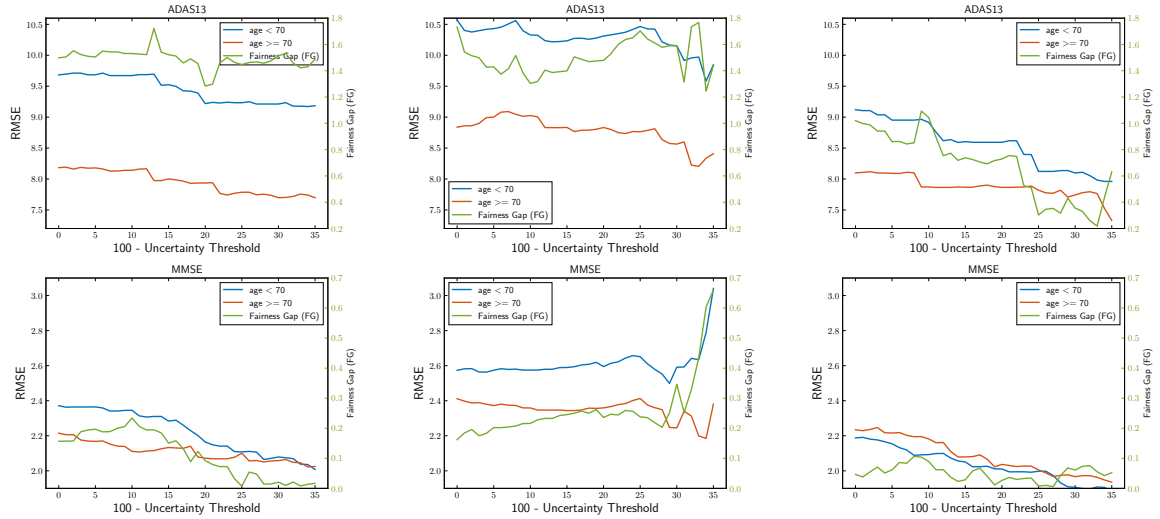

(a) (b) (c)

Figure 3: Root Mean Squared Error (RMSE) of ADAS-13 (Top) and MMSE (Bottom) scores as a function of (100-uncertainty threshold) for (a) **Baseline-Model**, (b) **Balanced-Model**, and (c) **GroupDRO-Model** on the ADNI dataset. Specifically, we plot RMSE for each subgroup (D^0 with age < 70 and D^1 with age ≥ 70). For Fairness Gap (FG) refer axis labels on the right.

is used as an evaluation metric (EM), where a lower value of RMSE represents better performance. Bayesian Deep Learning model with Ensemble Dropout (Smith and Gal, 2018) is used. A combination of Sample Variance and Predicted Variance, known as total variance (Kendall and Gal, 2017), is used to measure uncertainty associated with the model output.

Results: Figure 3 shows that compared to the **Baseline-Model**, the **Balanced-Model** only marginally decreases the fairness gap in the initial performance between two subgroups, that too at the cost of poor (higher RMSE) absolute performance for each of the subgroups. The **GroupDRO-Model** shows better absolute performance (lower RMSE) and also a lower fairness gap between each subgroup compared to either of the other two models. The **Baseline-Model** shows a decrease in the fairness gap between subgroups with a decrease in uncertainty threshold (moving from left to right) for MMSE, but it is not true for ADAS-13. On the contrary, the **Balanced-Model** shows an increase in the fairness gap with a decreased uncertainty threshold for both ADAS-13 and MMSE. The **GroupDRO-Model** gives the best performance as the fairness gap decreases with a decrease in uncertainty threshold for both ADAS-13 and MMSE.

4. Conclusions

Accurate uncertainty estimation of deep learning predictions in medical image analysis is necessary for their safe clinical deployment. In this paper, we presented the first exploration of fairness models in mitigating biases across subgroups, and their resulting effect on uncertainty quantification accuracy. Results on a wide range of experiments for three different tasks (classification, regression, and segmentation) indicate that popular fairness methods, such as data balancing and robust optimization, do not always work for different tasks. Futhermore, mitigating fairness in terms of performance can come at the cost of poor uncertainty estimation associated with output. As such, future work on overcoming these additional fairness issues is required prior to clinical deployment of these models.

Acknowledgments

Acknowledgments withheld.

References

Spyridon Bakas, Mauricio Reyes, Andras Jakab, Stefan Bauer, Markus Rempfler, Alessandro Crimi, Russell Takeshi Shinohara, Christoph Berger, Sung Min Ha, Martin Rozycki, et al. Identifying the best machine learning algorithms for brain tumor segmentation, progression assessment, and overall survival prediction in the brats challenge. *arXiv preprint arXiv:1811.02629*, 2018.

Neil Band, Tim GJ Rudner, Qixuan Feng, Angelos Filos, Zachary Nado, Michael W Dusenberry, Ghassen Jerfel, Dustin Tran, and Yarin Gal. Benchmarking bayesian deep learning on diabetic retinopathy detection tasks. In *Thirty-fifth Conference on Neural Information Processing Systems Datasets and Benchmarks Track (Round 2)*, 2021.

Philippe Burlina, Neil Joshi, William Paul, Katia D Pacheco, and Neil M Bressler. Addressing artificial intelligence bias in retinal diagnostics. *Translational Vision Science & Technology*, 10(2):13–13, 2021.

Özgün Çiçek, Ahmed Abdulkadir, Soeren S Lienkamp, Thomas Brox, and Olaf Ronneberger. 3d u-net: learning dense volumetric segmentation from sparse annotation. In *International conference on medical image computing and computer-assisted intervention*, pages 424–432. Springer, 2016.

Noel Codella, Veronica Rotemberg, Philipp Tschandl, M Emre Celebi, Stephen Dusza, David Gutman, Brian Helba, Aadi Kalloo, Konstantinos Liopyris, Michael Marchetti, et al. Skin lesion analysis toward melanoma detection 2018: A challenge hosted by the international skin imaging collaboration (isic). *arXiv preprint arXiv:1902.03368*, 2019.

Marshal F Folstein, Susan E Folstein, and Paul R McHugh. "mini-mental state": a practical method for grading the cognitive state of patients for the clinician. *Journal of psychiatric research*, 12(3):189–198, 1975.

Yarin Gal. Uncertainty in deep learning. 2016.

Yarin Gal and Zoubin Ghahramani. Dropout as a bayesian approximation: Representing model uncertainty in deep learning. In *international conference on machine learning*, pages 1050–1059, 2016.

Yarin Gal, Riashat Islam, and Zoubin Ghahramani. Deep bayesian active learning with image data. In *Proceedings of the 34th International Conference on Machine Learning-Volume 70*, pages 1183–1192. JMLR. org, 2017.

Florin C Ghesu, Bogdan Georgescu, Eli Gibson, Sebastian Guendel, Mannudeep K Kalra, Ramandeep Singh, Subba R Digumarthy, Sasa Grbic, and Dorin Comaniciu. Quantifying and leveraging classification uncertainty for chest radiograph assessment. In *International Conference on Medical Image Computing and Computer-Assisted Intervention*, pages 676–684. Springer, 2019.

Michel Goedert and Maria Grazia Spillantini. A century of alzheimer's disease. *science*, 314(5800):777–781, 2006.

Varun Gulshan, Lily Peng, Marc Coram, Martin C Stumpe, Derek Wu, Arunachalam Narayanaswamy, Subhashini Venugopalan, Kasumi Widner, Tom Madams, Jorge Cuadros, Ramasamy Kim, Rajiv Raman, Philip Q Nelson, Jessica Mega, and Dale Webster. Development and validation of a deep learning algorithm for detection of diabetic retinopathy in retinal fundus photographs. *JAMA*, 2016. URL http://jamanetwork.com/journals/jama/fullarticle/2588763.

Gery P Guy Jr, Cheryll C Thomas, Trevor Thompson, Meg Watson, Greta M Massetti, and Lisa C Richardson. Vital signs: melanoma incidence and mortality trends and projections—united states, 1982–2030. *Morbidity and mortality weekly report*, 64(21):591, 2015.

Kensho Hara, Hirokatsu Kataoka, and Yutaka Satoh. Can spatiotemporal 3d cnns retrace the history of 2d cnns and imagenet? In *Proceedings of the IEEE conference on Computer Vision and Pattern Recognition*, pages 6546–6555, 2018.

Kaiming He, Xiangyu Zhang, Shaoqing Ren, and Jian Sun. Deep residual learning for image recognition. In *Proceedings of the IEEE conference on computer vision and pattern recognition*, pages 770–778, 2016.

J Henry Hinnefeld, Peter Cooman, Nat Mammo, and Rupert Deese. Evaluating fairness metrics in the presence of dataset bias. *arXiv preprint arXiv:1809.09245*, 2018.

Badr Youbi Idrissi, Martin Arjovsky, Mohammad Pezeshki, and David Lopez-Paz. Simple data balancing achieves competitive worst-group-accuracy. In *Conference on Causal Learning and Reasoning*, pages 336–351. PMLR, 2022.

Stefanos Ioannou, Hana Chockler, Alexander Hammers, and Andrew P King. A study of demographic bias in cnn-based brain mr segmentation. In *International Workshop on Machine Learning in Clinical Neuroimaging*, pages 13–22. Springer, 2022.

Sergey Ioffe and Christian Szegedy. Batch normalization: Accelerating deep network training by reducing internal covariate shift. In *International conference on machine learning*, pages 448–456. PMLR, 2015.

Clifford R Jack Jr, Matt A Bernstein, Nick C Fox, Paul Thompson, Gene Alexander, Danielle Harvey, Bret Borowski, Paula J Britson, Jennifer L. Whitwell, Chadwick Ward, et al. The alzheimer's disease neuroimaging initiative (adni): Mri methods. *Journal of Magnetic Resonance Imaging: An Official Journal of the International Society for Magnetic Resonance in Medicine*, 27(4):685–691, 2008.

Nathalie Japkowicz and Shaju Stephen. The class imbalance problem: A systematic study. *Intelligent data analysis*, 6(5):429–449, 2002.

Alain Jungo and Mauricio Reyes. Assessing reliability and challenges of uncertainty estimations for medical image segmentation. In *International Conference on Medical Image Computing and Computer-Assisted Intervention*, pages 48–56. Springer, 2019.

Alex Kendall and Yarin Gal. What uncertainties do we need in bayesian deep learning for computer vision? *arXiv preprint arXiv:1703.04977*, 2017.

Diederik P Kingma and Jimmy Ba. Adam: A method for stochastic optimization. *arXiv preprint arXiv:1412.6980*, 2014.

Balaji Lakshminarayanan, Alexander Pritzel, and Charles Blundell. Simple and scalable predictive uncertainty estimation using deep ensembles. In *Advances in neural information processing systems*, pages 6402–6413, 2017.

Agostina J Larrazabal, Nicolás Nieto, Victoria Peterson, Diego H Milone, and Enzo Ferrante. Gender imbalance in medical imaging datasets produces biased classifiers for computer-aided diagnosis. *Proceedings of the National Academy of Sciences*, 117(23): 12592–12594, 2020.

Ninareh Mehrabi, Fred Morstatter, Nripsuta Saxena, Kristina Lerman, and Aram Galstyan. A survey on bias and fairness in machine learning. *ACM Computing Surveys (CSUR)*, 54(6):1–35, 2021.

Raghav Mehta and Tal Arbel. Rs-net: Regression-segmentation 3d cnn for synthesis of full resolution missing brain mri in the presence of tumours. In *International Workshop on Simulation and Synthesis in Medical Imaging*, pages 119–129. Springer, 2018.

Raghav Mehta, Angelos Filos, Ujjwal Baid, Chiharu Sako, Richard McKinley, Michael Rebsamen, Katrin Dätwyler, Raphael Meier, Piotr Radojewski, Gowtham Krishnan Murugesan, et al. Qu-brats: Miccai brats 2020 challenge on quantifyinguncertainty in brain tumor segmentation-analysis of ranking scores and benchmarking results. *Journal of Machine Learning for Biomedical Imaging*, 1, 2022.

Pieter Van Molle, Tim Verbelen, Cedric De Boom, Bert Vankeirsbilck, Jonas De Vylder, Bart Diricx, Tom Kimpe, Pieter Simoens, and Bart Dhoedt. Quantifying uncertainty of deep neural networks in skin lesion classification. In *Uncertainty for Safe Utilization of Machine Learning in Medical Imaging and Clinical Image-Based Procedures*, pages 52–61. Springer, 2019.

Tanya Nair, Doina Precup, Douglas L Arnold, and Tal Arbel. Exploring uncertainty measures in deep networks for multiple sclerosis lesion detection and segmentation. *Medical image analysis*, 59:101557, 2020.

Radford M Neal. *Bayesian learning for neural networks*, volume 118. Springer Science & Business Media, 2012.

Adam Paszke, Sam Gross, Francisco Massa, Adam Lerer, James Bradbury, Gregory Chanan, Trevor Killeen, Zeming Lin, Natalia Gimelshein, Luca Antiga, et al. Pytorch: An imperative style, high-performance deep learning library. *Advances in neural information processing systems*, 32, 2019.

Esther Puyol-Antón, Bram Ruijsink, Stefan K Piechnik, Stefan Neubauer, Steffen E Petersen, Reza Razavi, and Andrew P King. Fairness in cardiac mr image analysis: an

investigation of bias due to data imbalance in deep learning based segmentation. In *International Conference on Medical Image Computing and Computer-Assisted Intervention*, pages 413–423. Springer, 2021.

María Agustina Ricci Lara, Rodrigo Echeveste, and Enzo Ferrante. Addressing fairness in artificial intelligence for medical imaging. *nature communications*, 13(1):1–6, 2022.

Wilma G Rosen, Richard C Mohs, and Kenneth L Davis. A new rating scale for alzheimer's disease. *The American journal of psychiatry*, 1984.

Shiori Sagawa, Pang Wei Koh, Tatsunori B Hashimoto, and Percy Liang. Distributionally robust neural networks for group shifts: On the importance of regularization for worst-case generalization. *arXiv preprint arXiv:1911.08731*, 2019.

Laleh Seyyed-Kalantari, Haoran Zhang, Matthew McDermott, Irene Y Chen, and Marzyeh Ghassemi. Underdiagnosis bias of artificial intelligence algorithms applied to chest radiographs in under-served patient populations. *Nature medicine*, 27(12):2176–2182, 2021.

Lewis Smith and Yarin Gal. Understanding measures of uncertainty for adversarial example detection. *arXiv preprint arXiv:1803.08533*, 2018.

Nitish Srivastava, Geoffrey Hinton, Alex Krizhevsky, Ilya Sutskever, and Ruslan Salakhutdinov. Dropout: a simple way to prevent neural networks from overfitting. *The journal of machine learning research*, 15(1):1929–1958, 2014.

Ryutaro Tanno, Daniel E Worrall, Enrico Kaden, Aurobrata Ghosh, Francesco Grussu, Alberto Bizzi, Stamatios N Sotiropoulos, Antonio Criminisi, and Daniel C Alexander. Uncertainty modelling in deep learning for safer neuroimage enhancement: demonstration in diffusion mri. *NeuroImage*, 225:117366, 2021.

Dmitry Ulyanov, Andrea Vedaldi, and Victor Lempitsky. Instance normalization: The missing ingredient for fast stylization. *arXiv preprint arXiv:1607.08022*, 2016.

Yongshuo Zong, Yongxin Yang, and Timothy Hospedales. Medfair: Benchmarking fairness for medical imaging. *arXiv preprint arXiv:2210.01725*, 2022.

Appendix A. Multi-Class Skin Lesion Classification

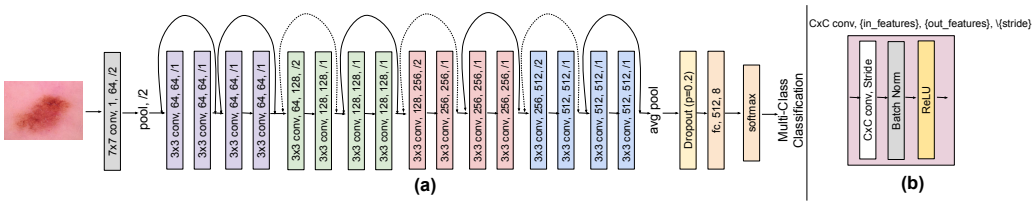

Figure 4: (a) A 2D ResNet-18 architecture consists of a 7x7 convolutional unit, followed by 16 3x3 convolutional units, one dropout layer (p=0.2), and one fully connected layers. The dotted shortcuts increase dimensions. (b) Each convolutional unit consists of one CxC convolutional layer with stride S, followed by Batch Normalization layer (Ioffe and Szegedy, 2015), and a ReLU layer.

Implementation Details: An ImageNet pre-trained 2D ResNet18 (He et al., 2016) architecture was used for the ISIC multi-class disease scale classification task. The network architecture is depicted in Figure-4. A Dropout layer (Srivastava et al., 2014) with p=0.2 is introduced before the fully connected (fc) layer. The network was trained to reduce the categorical cross entropy loss. An Adam optimizer (Kingma and Ba, 2014) with a learning rate of 0.0005 and a weight decay of 0.00001 was used to train the network for a total of 100 epochs, and batch size of 64. The learning rate was decayed with a factor of 0.995 after each epoch. All ISIC images were resized to 600x450 size and normalized with mean subtraction and divide by std. Random Horizontal Flip, Random Vertical Flip, and Random rotation in the range of 0-30, was applied as data augmentation on each image. The code was written in PyTorch (Paszke et al., 2019) and ran on Nvidia GeForce RTX 3090 GPU with 24GB memory. For generating EnsembleDropout (Smith and Gal, 2018), we train three different networks with different random initialization of network weights and take 20 MC-Dropout samples (Gal and Ghahramani, 2016) from each. This results in a total of 60 Monte-Carlo samples for each image.

	ISIC Dataset								
	Melanoma	**Melanocytic Nevus**	**Basal Cell Carcinoma**	**Actinic Keratosis**	**Benign Keratosis**	**Dermatofibroma**	**Vascular Lesion**	**Squamous Cell Carcinoma**	**Total**
D^0	2593	2600	2387	707	1785	79	108	546	10805
D^1	1844	9958	930	157	813	160	145	82	14045
Overall	4437	12558	3317	864	2598	239	253	628	24850

Table 1: Number of images for each class and each subgroup for the whole ISIC dataset. From this, we can see a high-class imbalance across different classes. Similarly, distribution across both subgroups for a particular class is also different. For example, while for Melanoma, Basal Cell Carcinoma, Actinic Keratosis, Benign Keratosis, and Squamous Cell Carcinoma, D^0 has a higher number of samples compared to D^1, for the rest of the classes (Melanocytic Nevus, Dermatofibroma, and Vascular Lesion) D^1 has a higher number of samples compared to D^0.

	Training Dataset (Baseline-Model and GroupDRO-Model)								
	Melanoma	**Melanocytic Nevus**	**Basal Cell Carcinoma**	**Actinic Keratosis**	**Benign Keratosis**	**Dermatofibroma**	**Vascular Lesion**	**Squamous Cell Carcinoma**	**Total**
D^0	1835	1638	1895	594	1388	50	68	470	7938
D^1	1161	8280	585	99	513	122	100	52	10912
Overall	2996	9918	2480	693	1901	172	168	522	18850

Table 2: Number of images for each class and each subgroup for the training dataset used to train the **Baseline-Model** and the **GroupDRO-Model**. Similar to the whole ISIC dataset (Table-1), we see high-class imbalance across different classes, and different distributions across both subgroups for a particular class.

	Training Dataset (Balanced-Model)								
	Melanoma	**Melanocytic Nevus**	**Basal Cell Carcinoma**	**Actinic Keratosis**	**Benign Keratosis**	**Dermatofibroma**	**Vascular Lesion**	**Squamous Cell Carcinoma**	**Total**
D^0	1161	1638	585	99	513	50	68	52	4166
D^1	1161	1638	585	99	513	50	68	52	4166
Overall	2322	3276	1170	198	1026	100	136	104	8332

Table 3: Number of images for each class and each subgroup for the training dataset used to train the **Balanced-Model**. Compared to the training dataset used for the **Baseline-Model** and the **GroupDRO-Model** (Table-2), we balance the number of samples across both subgroups, but we do not balance across different classes.

	Validation Dataset (Baseline-Model, GroupDRO-Model, and Balanced-Model)								
	Melanoma	**Melanocytic Nevus**	**Basal Cell Carcinoma**	**Actinic Keratosis**	**Benign Keratosis**	**Dermatofibroma**	**Vascular Lesion**	**Squamous Cell Carcinoma**	**Total**
D^0	204	182	212	66	154	5	7	52	882
D^1	129	918	65	11	57	14	12	6	1212
Overall	333	1100	277	77	211	19	19	58	2094

Table 4: Number of images for each class and each subgroup in the Validation dataset for all three models (the **Baseline-Model** and the **GroupDRO-Model**, and the **Balanced-Model)**. The distribution of samples across both subgroups and across different classes is similar to the Table-1.

	Testing Dataset (Baseline-Model, GroupDRO-Model, and Balanced-Model)								
	Melanoma	**Melanocytic Nevus**	**Basal Cell Carcinoma**	**Actinic Keratosis**	**Benign Keratosis**	**Dermatofibroma**	**Vascular Lesion**	**Squamous Cell Carcinoma**	**Total**
D^0	554	780	280	47	243	24	33	24	1985
D^1	554	780	280	47	243	24	33	24	1985
Overall	1108	1560	560	94	486	48	66	48	3970

Table 5: Number of images for each class and each subgroup in the Testing dataset used to test all three models (the **Baseline-Model** and the **GroupDRO-Model**, and the **Balanced-Model)**. The distribution of samples across both subgroups is kept similar, but it is not similar across different classes. We kept similar distribution across both subgroups for a fair comparison of their performance, while the distribution across different classes was not kept similar to reflect real-world scenarios where some classes can be more frequent compared to others.

Baseline-Model	AUC	Accuracy	Balanced-Accuracy
D^0	96.46	78.74	72.64
D^1	95.71	76.83	66.76
Fairness Gap	0.75	1.91	5.88

Table 6: Overall metrics (AUC, Accuracy, and Balanced-Accuracy) for a **Baseline-Model** trained on the ISIC dataset at $\tau = 100$.

Balanced-Model	AUC	Accuracy	Balanced-Accuracy
D^0	93.91	77.28	63.70
D^1	95.09	76.68	66.87
Fairness Gap	1.18	0.60	3.17

Table 7: Overall metrics (AUC, Accuracy, and Balanced-Accuracy) for a **Balanced-Model** trained on the ISIC dataset at $\tau = 100$.

GroupDRO-Model	AUC	Accuracy	Balanced-Accuracy
D^0	96.20	79.55	71.95
D^1	95.95	78.38	71.33
Fairness Gap	0.25	1.17	0.62

Table 8: Overall metrics (AUC, Accuracy, and Balanced-Accuracy) for a **GroupDRO-Model** trained on the ISIC dataset at $\tau = 100$.

Baseline-Model	Class-level Accuracy							
	Melanoma	Melanocytic Nevus	Basal Cell Carcinoma	Actinic Keratosis	Benign Keratosis	Dermatofibroma	Vascular Lesion	Squamous Cell Carcinoma
D^0	75.09	86.03	81.43	61.70	66.67	54.17	72.73	83.33
D^1	64.62	91.41	77.86	65.96	64.20	25.00	90.91	54.17
Fairness Gap	10.47	5.38	3.57	4.26	2.47	29.17	18.18	29.16

Table 9: Per class accuracy for a **Baseline-Model** trained on the ISIC dataset at $\tau = 100$.

Balanced-Model	Class-level Accuracy							
	Melanoma	Melanocytic Nevus	Basal Cell Carcinoma	Actinic Keratosis	Benign Keratosis	Dermatofibroma	Vascular Lesion	Squamous Cell Carcinoma
D^0	75.09	83.33	86.78	38.30	66.26	58.33	84.85	16.67
D^1	74.37	79.87	87.50	57.45	68.72	58.33	87.88	20.83
Fairness Gap	0.72	3.46	0.72	19.15	2.46	0.00	3.03	4.16

Table 10: Per class accuracy for a **Balanced-Model** trained on the ISIC dataset at $\tau = 100$.

GroupDRO-Model	Class-level Accuracy							
	Melanoma	Melanocytic Nevus	Basal Cell Carcinoma	Actinic Keratosis	Benign Keratosis	Dermatofibroma	Vascular Lesion	Squamous Cell Carcinoma
D^0	79.96	81.02	88.93	57.45	71.61	45.83	75.76	75.00
D^1	68.23	87.69	86.43	85.11	66.67	29.17	84.85	62.50
Fairness Gap	11.73	6.67	2.50	27.66	4.94	16.66	9.09	12.50

Table 11: Per class accuracy for a **GroupDRO-Model** trained on the ISIC dataset at $\tau = 100$.

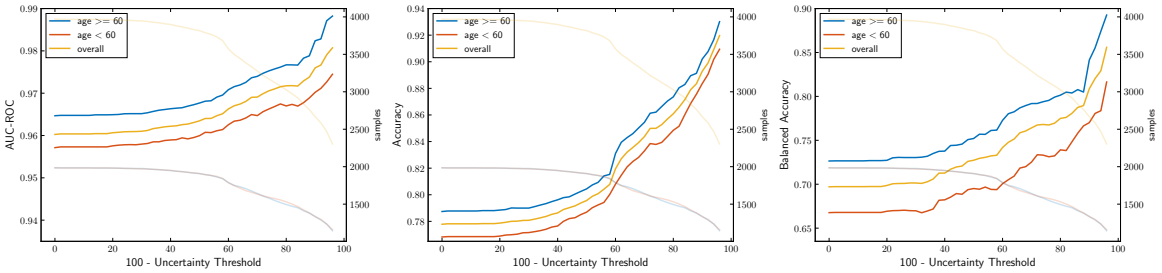

(a) Baseline Model

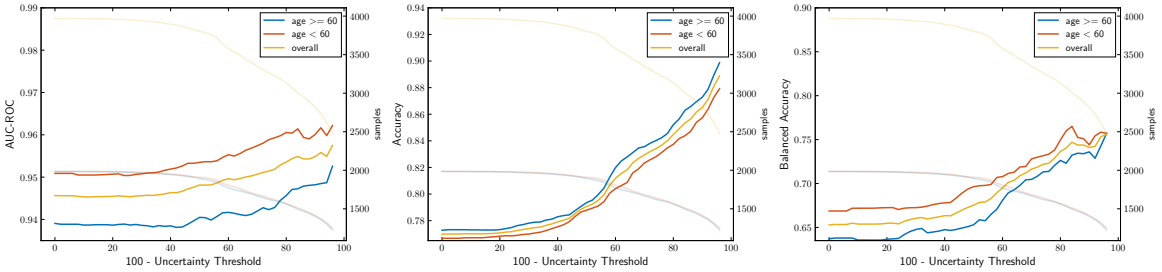

(b) Balanced Model

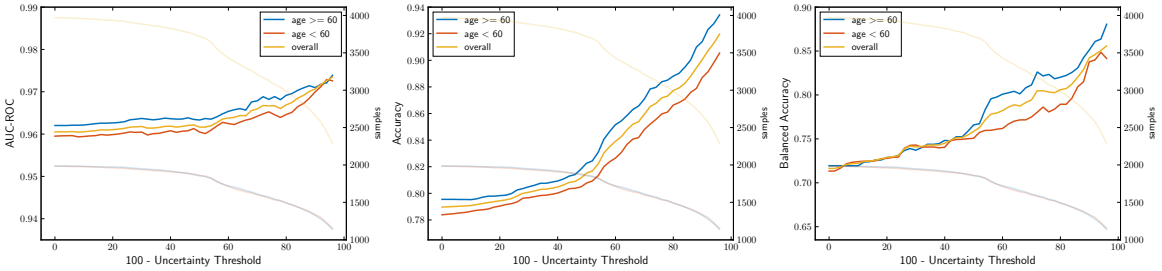

(c) GroupDRO Model

Figure 5: **ISIC:** Overall AUC, accuracy, and Balanced Accuracy as a function of uncertainty threshold for (a) **Baseline-Model**, (b) **Balanced-Model**, and (c) **GroupDRO-Model** on the ISIC dataset. In addition to metrics, the total number of testing images for each subgroup (D^0 - age $>= 60$ and D^1 - age < 60) are shown as light colours.

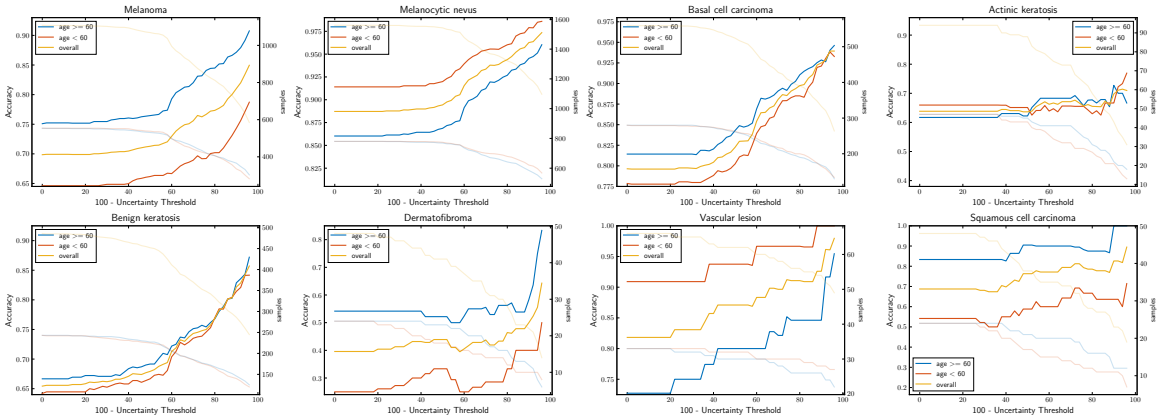

(a) Baseline Model

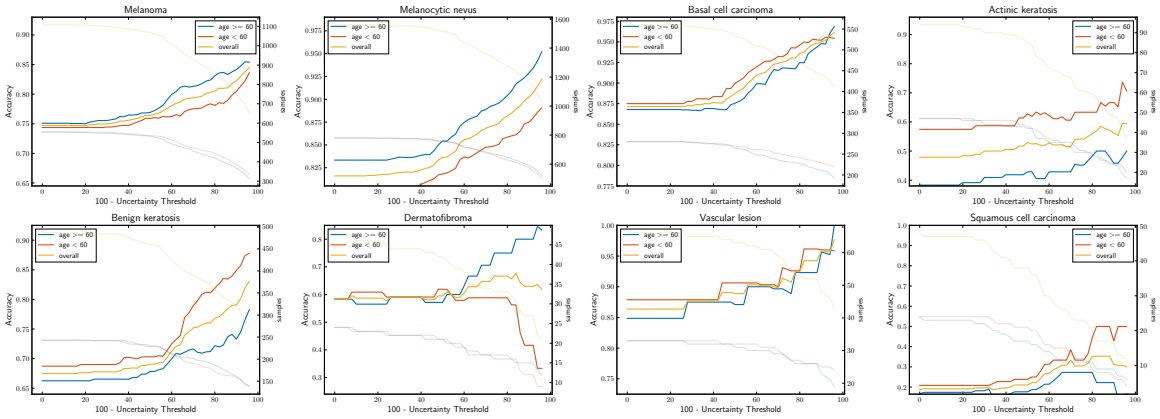

(b) Balanced Model

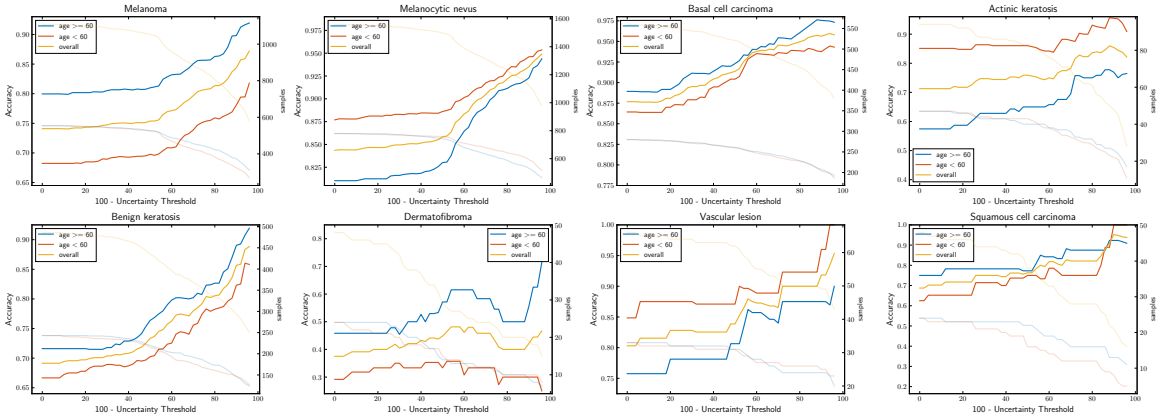

(c) GroupDRO Model

Figure 6: **ISIC:** Class-level accuracy as a function of uncertainty threshold for (a) **Baseline-Model**, (b) **Balanced-Model**, and (c) **GroupDRO-Model** on the ISIC dataset. In addition to the accuracy, the total number of testing images for each subgroup (D^0 - age $>= 60$ and D^1 - age < 60) are shown as light colours.

A.1. ISIC - Sex as a sensitive attribute

We use sex as a sensitive attribute for experiments in this section. Specifically, we divide the ISIC dataset into two subsets based on the sex associated with each image (male vs female). The entire dataset is divided into two subsets: patient images from female patients in subgroup D^0 with a total of 11661 images, and patient images from male patients in subgroup D^1 with a total of 13286 images.

	ISIC Dataset								
	Melanoma	**Melanocytic Nevus**	**Basal Cell Carcinoma**	**Actinic Keratosis**	**Benign Keratosis**	**Dermatofibroma**	**Vascular Lesion**	**Squamous Cell Carcinoma**	**Total**
D^0	1980	6379	1317	406	1134	117	125	203	11661
D^1	2461	6225	2000	458	1467	122	128	425	13286
Overall	4441	12604	3317	864	2601	239	253	628	24947

Table 12: Number of images for each class and each subgroup for the whole ISIC dataset. From this, we can see a high-class imbalance across different classes. Similarly, distribution across both subgroups for a particular class is also different. For example, while for Melanoma, Basal Cell Carcinoma, Actinic Keratosis, Benign Keratosis, and Squamous Cell Carcinoma, D^0 has a higher number of samples compared to D^1, for the rest of the classes (Melanocytic Nevus, Dermatofibroma, and Vascular Lesion) D^1 has a higher number of samples compared to D^0.

	Training Dataset (Baseline-Model and GroupDRO-Model)								
	Melanoma	**Melanocytic Nevus**	**Basal Cell Carcinoma**	**Actinic Keratosis**	**Benign Keratosis**	**Dermatofibroma**	**Vascular Lesion**	**Squamous Cell Carcinoma**	**Total**
D^0	1248	4061	830	257	715	73	78	128	7390
D^1	1680	3922	1445	303	1015	78	81	328	8852
Overall	2928	7983	2275	560	1730	151	159	456	16242

Table 13: Number of images for each class and each subgroup for the training dataset used to train the **Baseline-Model** and the **GroupDRO-Model**. Similar to the whole ISIC dataset (Table-12), we see high-class imbalance across different classes, and different distributions across both subgroups for a particular class.

	Training Dataset (Balanced-Model)								
	Melanoma	**Melanocytic Nevus**	**Basal Cell Carcinoma**	**Actinic Keratosis**	**Benign Keratosis**	**Dermatofibroma**	**Vascular Lesion**	**Squamous Cell Carcinoma**	**Total**
D^0	1248	3922	830	257	715	73	78	128	7251
D^1	1248	3922	830	257	715	73	78	128	7251
Overall	2496	7844	1660	514	1430	146	156	256	14502

Table 14: Number of images for each class and each subgroup for the training dataset used to train the **Balanced-Model**. Compared to the training dataset used for the **Baseline-Model** and the **GroupDRO-Model** (Table-13), we balance the number of samples across both subgroups, but we do not balance across different classes.

	Validation Dataset (Baseline-Model, GroupDRO-Model, and Balanced-Model)								
	Melanoma	**Melanocytic Nevus**	**Basal Cell Carcinoma**	**Actinic Keratosis**	**Benign Keratosis**	**Dermatofibroma**	**Vascular Lesion**	**Squamous Cell Carcinoma**	**Total**
D^0	138	451	92	28	79	8	9	14	819
D^1	187	436	160	34	112	8	9	36	982
Overall	325	887	252	62	191	16	18	50	1801

Table 15: Number of images for each class and each subgroup in the Validation dataset for all three models (the **Baseline-Model** and the **GroupDRO-Model**, and the **Balanced-Model)**. The distribution of samples across both subgroups and across different classes is similar to the Table-12.

	Testing Dataset (Baseline-Model, GroupDRO-Model, and Balanced-Model)								
	Melanoma	**Melanocytic Nevus**	**Basal Cell Carcinoma**	**Actinic Keratosis**	**Benign Keratosis**	**Dermatofibroma**	**Vascular Lesion**	**Squamous Cell Carcinoma**	**Total**
D^0	594	1867	395	121	340	36	38	61	3452
D^1	594	1867	395	121	340	36	38	61	3452
Overall	1188	3734	790	242	680	72	76	122	6904

Table 16: Number of images for each class and each subgroup in the Testing dataset used to test all three models (the **Baseline-Model** and the **GroupDRO-Model**, and the **Balanced-Model)**. The distribution of samples across both subgroups is kept similar, but it is not similar across different classes. We kept similar distribution across both subgroups for a fair comparison of their performance, while the distribution across different classes was not kept similar to reflect real-world scenarios where some classes can be more frequent compared to others.

Baseline-Model	**AUC**	**Accuracy**	**Balanced-Accuracy**
D^0	96.24	83.02	71.77
D^1	96.83	83.02	70.23
Fairness Gap	0.59	0.00	1.54

Table 17: Overall metrics (AUC, Accuracy, and Balanced-Accuracy) for a **Baseline-Model** trained on the ISIC dataset at $\tau = 100$.

Balanced-Model	**AUC**	**Accuracy**	**Balanced-Accuracy**
D^0	96.26	82.24	70.26
D^1	95.92	81.66	69.42
Fairness Gap	0.34	0.58	0.74

Table 18: Overall metrics (AUC, Accuracy, and Balanced-Accuracy) for a **Balanced-Model** trained on the ISIC dataset at $\tau = 100$.

GroupDRO-Model	**AUC**	**Accuracy**	**Balanced-Accuracy**
D^0	95.76	80.56	70.25
D^1	96.31	80.59	69.90
Fairness Gap	0.55	0.03	0.35

Table 19: Overall metrics (AUC, Accuracy, and Balanced-Accuracy) for a **GroupDRO-Model** trained on the ISIC dataset at $\tau = 100$.

Baseline-Model	Class-level Accuracy							
	Melanoma	Melanocytic Nevus	Basal Cell Carcinoma	Actinic Keratosis	Benign Keratosis	Dermatofibroma	Vascular Lesion	Squamous Cell Carcinoma
D^0	65.32	91.64	85.06	61.16	80.29	63.88	71.05	55.74
D^1	73.91	91.27	87.09	52.07	68.53	44.44	92.11	52.46
Fairness Gap	8.59	0.37	2.03	9.09	11.76	19.44	21.06	3.28

Table 20: Per class accuracy for a **Baseline-Model** trained on the ISIC dataset at $\tau = 100$.

Balanced-Model	Class-level Accuracy							
	Melanoma	Melanocytic Nevus	Basal Cell Carcinoma	Actinic Keratosis	Benign Keratosis	Dermatofibroma	Vascular Lesion	Squamous Cell Carcinoma
D^0	62.79	92.34	88.35	59.50	70.88	66.67	78.95	42.62
D^1	68.52	90.95	87.59	54.55	65.88	61.11	94.74	32.79
Fairness Gap	5.73	1.39	0.76	4.95	5.00	5.56	15.79	9.83

Table 21: Per class accuracy for a **Balanced-Model** trained on the ISIC dataset at $\tau = 100$.

GroupDRO-Model	Class-level Accuracy							
	Melanoma	Melanocytic Nevus	Basal Cell Carcinoma	Actinic Keratosis	Benign Keratosis	Dermatofibroma	Vascular Lesion	Squamous Cell Carcinoma
D^0	55.05	92.07	83.29	66.12	70.29	55.56	78.95	60.66
D^1	63.13	90.52	82.28	59.50	68.24	50.00	81.58	63.93
Fairness Gap	8.08	1.55	1.01	6.62	2.05	5.56	2.63	3.27

Table 22: Per class accuracy for a **GroupDRO-Model** trained on the ISIC dataset at $\tau = 100$.

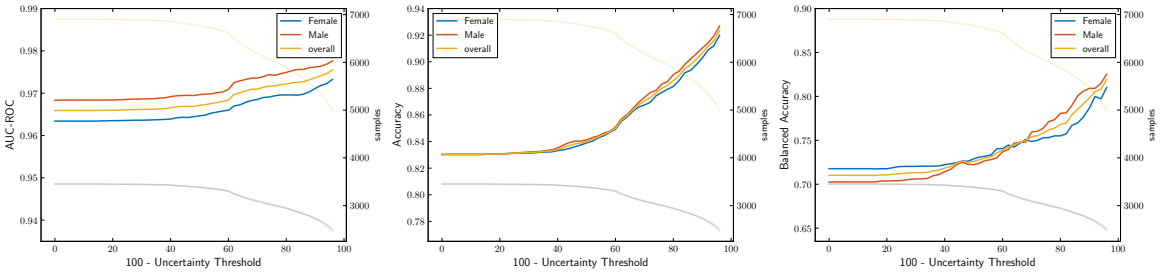

(a) Baseline Model

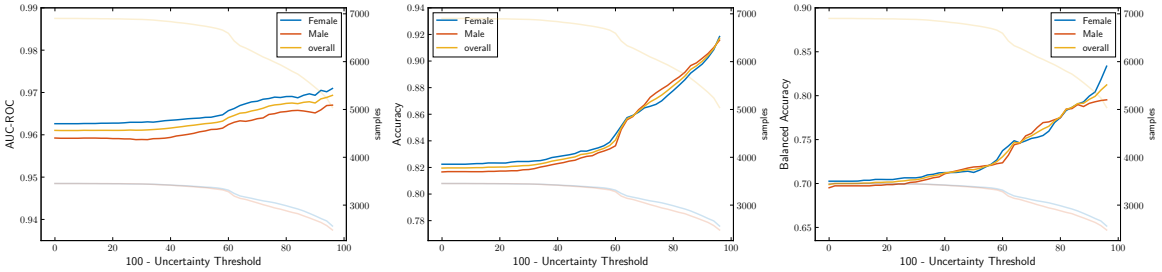

(b) Balanced Model

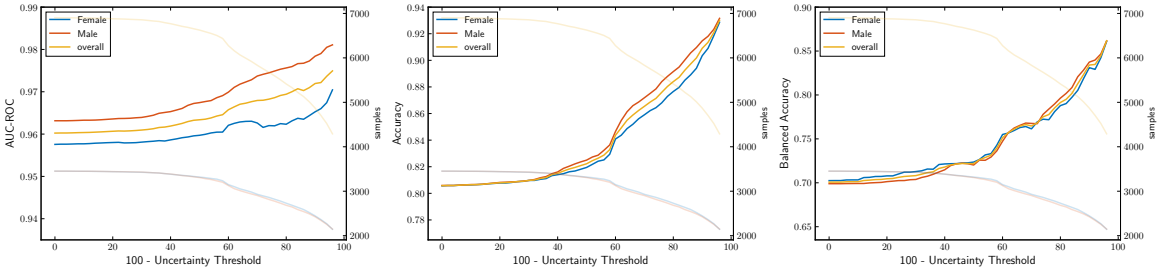

(c) GroupDRO Model

Figure 7: **ISIC-Sex:** Overall AUC, accuracy, and Balanced Accuracy as a function of uncertainty threshold for (a) **Baseline-Model**, (b) **Balanced-Model**, and (c) **GroupDRO-Model** on the ISIC dataset. In addition to metrics, the total number of testing images for each subgroup (D^0 - Female and D^1 - Male) are shown as light colours.

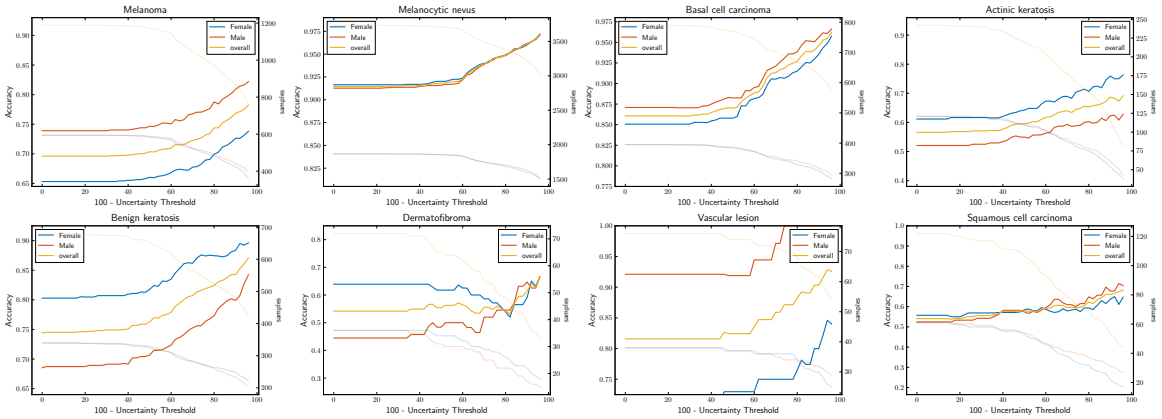

(a) Baseline Model

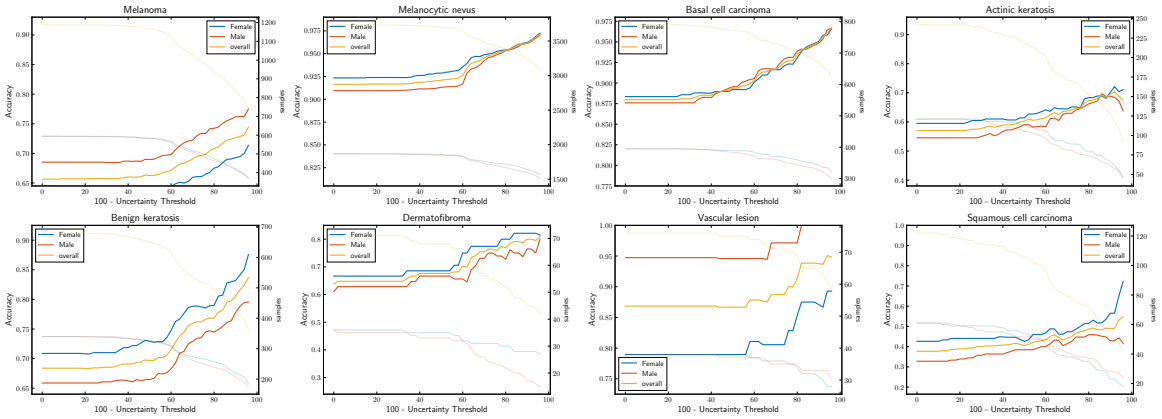

(b) Balanced Model

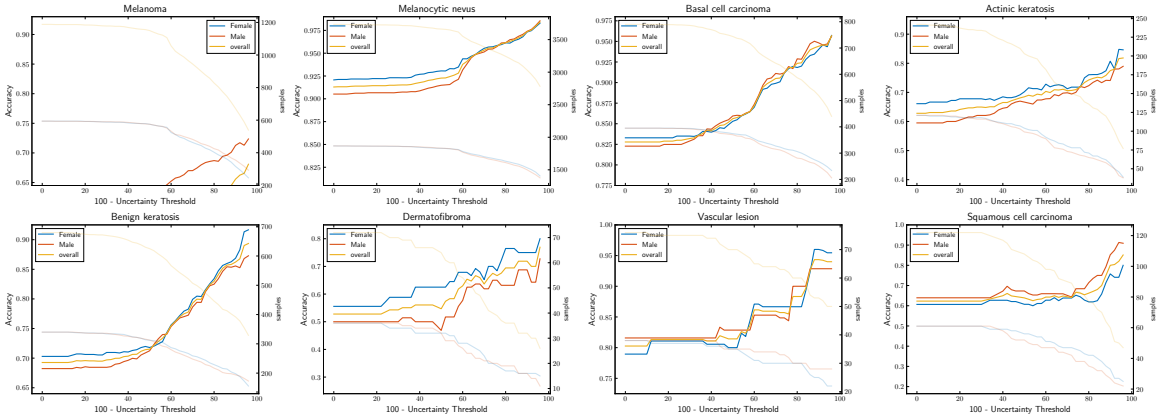

(c) GroupDRO Model

Figure 8: **ISIC-Sex:** Class-level accuracy as a function of uncertainty threshold for (a) **Baseline-Model**, (b) **Balanced-Model**, and (c) **GroupDRO-Model** on the ISIC dataset. In addition to the accuracy, the total number of testing images for each subgroup (D^0 - Female and D^1 - Male) are shown as light colours.

Appendix B. Brain Tumour Segmentation

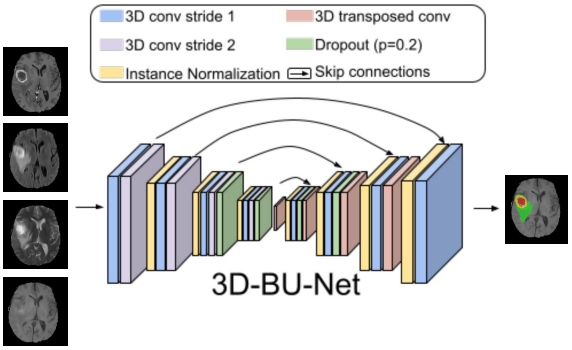

Figure 9: Network architecture diagram of the modified 3D-BU-Net (Nair et al., 2020), used for the multi-class brain tumour segmentation. It takes multi-modal MR images as input and produces multi brain tumour segmentation on the BraTS dataset.

Implementation Details: We use a BU-Net (Nair et al., 2020) architecture for brain tumour segmentation on the BraTS dataset. Similar to the original 3D BU-Net, the network consists of encoder and decoder paths that embed convolution and deconvolution operations. High-resolution features from the encoder path were combined with the up-sampled output of the decoder to preserve high-resolution features. Each convolution was followed by rectified linear unit activation (ReLU). Instead of using the batch-normalization layer used in the original U-Net, we used instance normalization (Ulyanov et al., 2016). Instance normalization typically improves performance for small batch sizes. The network was trained using Adam (Kingma and Ba, 2014) optimizer with a learning rate of 0.0002 and weight decay of 0.00001 for a total of 240 epochs to minimize weighted cross-entropy loss. Here, the weights are defined such that the weight increases whenever there are fewer voxels in a particular class. After every epoch, class weights were decayed with a factor of 0.95, which results in equally weighted binary cross-entropy after around 50 epochs. The code was written in PyTorch (Paszke et al., 2019) and ran on Nvidia GeForce RTX 3090 GPU with 24GB memory. For generating EnsembleDropout (Smith and Gal, 2018), we train three different networks with different random initialization of network weights and take 20 MC-Dropout samples (Gal and Ghahramani, 2016) from each. This results in a total of 60 Monte-Carlo samples for each image.

	Training Set		Validation Set	Testing Set	BraTS Dataset
	Baseline-Model and GroupDRO-Model	Balanced Model			
D^0	168	30	18	20	206
D^1	30	30	4	20	54
Overall	198	60	22	40	260

Table 23: Number of samples in both D^0 and D^1 subgroups for five different datasets: (i) Training Dataset used to train the **Baseline-Model** and the **GroupDRO-Model**, (ii) Training Dataset used to the train the **Balanced-Model**, (iii) Validation set for all three models, (iv) Testing set for all three models, and (v) for the whole BraTS dataset. We can observe that for the BraTS dataset, there is a high disparity between the number of samples for both subgroups.

Baseline-Model	Dice			QU-BraTS Metric		
	Whole Tumour	Tumour Core	Enhancing Tumour	Whole Tumour	Tumour Core	Enhancing Tumour
D^0	90.34	85.14	81.80	92.50	88.81	82.90
D^1	86.99	70.33	56.13	89.37	76.11	75.05
Fairness Gap	3.35	14.81	25.67	3.13	12.70	7.85

Table 24: Dice (at $\tau = 100$) and QU-BraTS metric (Mehta et al., 2022) values for Whole Tumour, Tumour Core, and Enhancing Tumour of a **Baseline-Model** on the BraTS dataset.

Balanced-Model	Dice			QU-BraTS Metric		
	Whole Tumour	Tumour Core	Enhancing Tumour	Whole Tumour	Tumour Core	Enhancing Tumour
D^0	82.33	74.94	73.92	86.67	77.68	71.08
D^1	83.45	68.19	48.96	86.24	74.44	71.93
Fairness Gap	1.12	6.75	24.96	0.43	3.24	0.85

Table 25: Dice (at $\tau = 100$) and QU-BraTS metric (Mehta et al., 2022) values for Whole Tumour, Tumour Core, and Enhancing Tumour of a **Balanced-Model** on the BraTS dataset.

GroupDRO-Model	Dice			QU-BraTS Metric		
	Whole Tumour	Tumour Core	Enhancing Tumour	Whole Tumour	Tumour Core	Enhancing Tumour
D^0	90.02	86.80	83.16	92.07	89.84	89.33
D^1	86.47	62.64	60.14	90.30	77.42	73.17
Fairness Gap	3.55	24.16	23.02	1.77	12.42	16.16

Table 26: Dice (at $\tau = 100$) and QU-BraTS metric (Mehta et al., 2022) values for Whole Tumour, Tumour Core, and Enhancing Tumour of a **GroupDRO-Model** on the BraTS dataset.

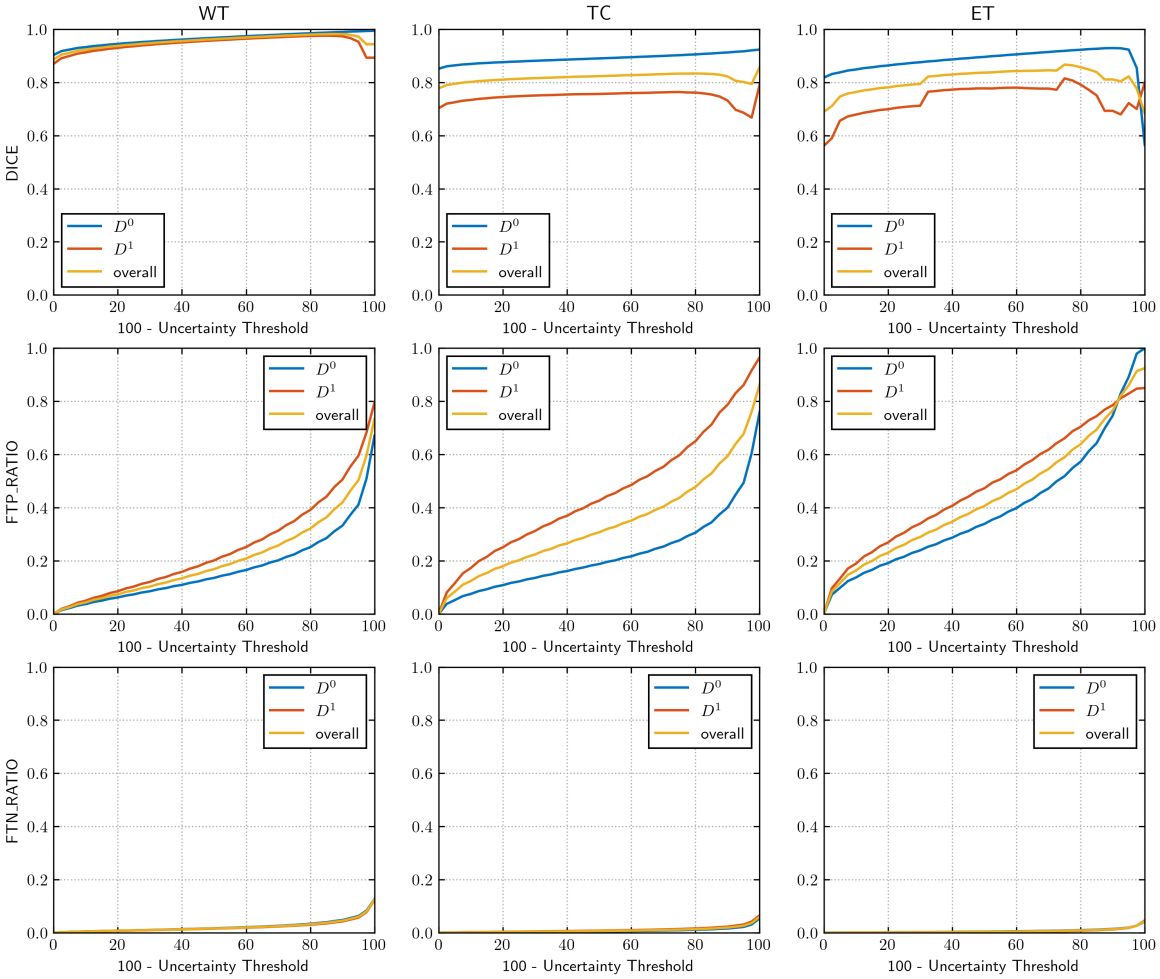

Figure 10: **BraTS:** Dice, Filtered True Positive Ratio (FTP), and Filtered True Negative Ratio (FTN) as a function of uncertainty threshold for **Baseline-Model** on the BraTS dataset. Specifically, we plot Whole Tumour (WT), Tumour Core (TC), and Enhancing Tumour (ET) QU-BraTS (Mehta et al., 2022) metrics for both the D^0 and D^1 set.

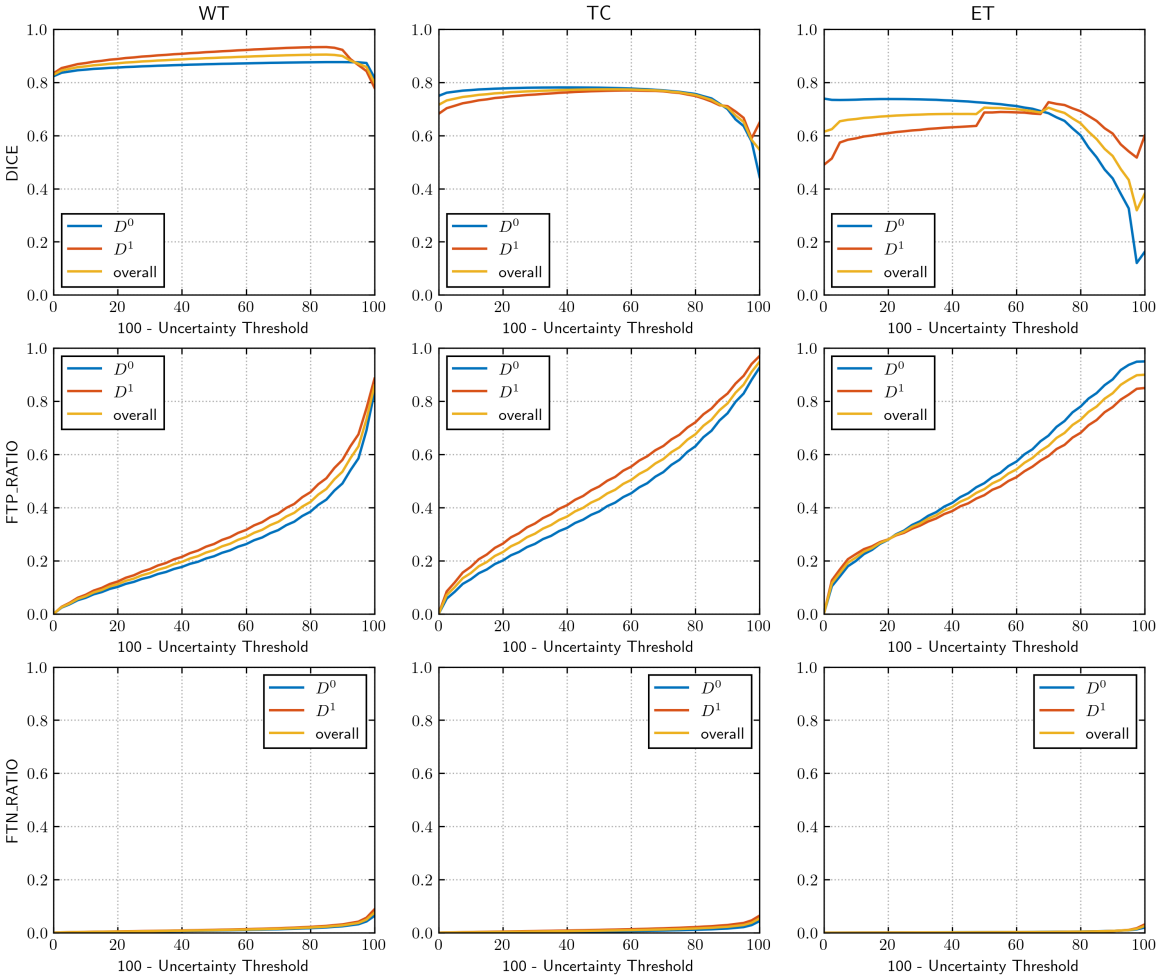

Figure 11: **BraTS:** Dice, Filtered True Positive Ratio (FTP), and Filtered True Negative Ratio (FTN) as a function of uncertainty threshold for **Balanced-Model** on the BraTS dataset. Specifically, we plot Whole Tumour (WT), Tumour Core (TC), and Enhancing Tumour (ET) QU-BraTS (Mehta et al., 2022) metrics for both the D^0 and D^1 set..

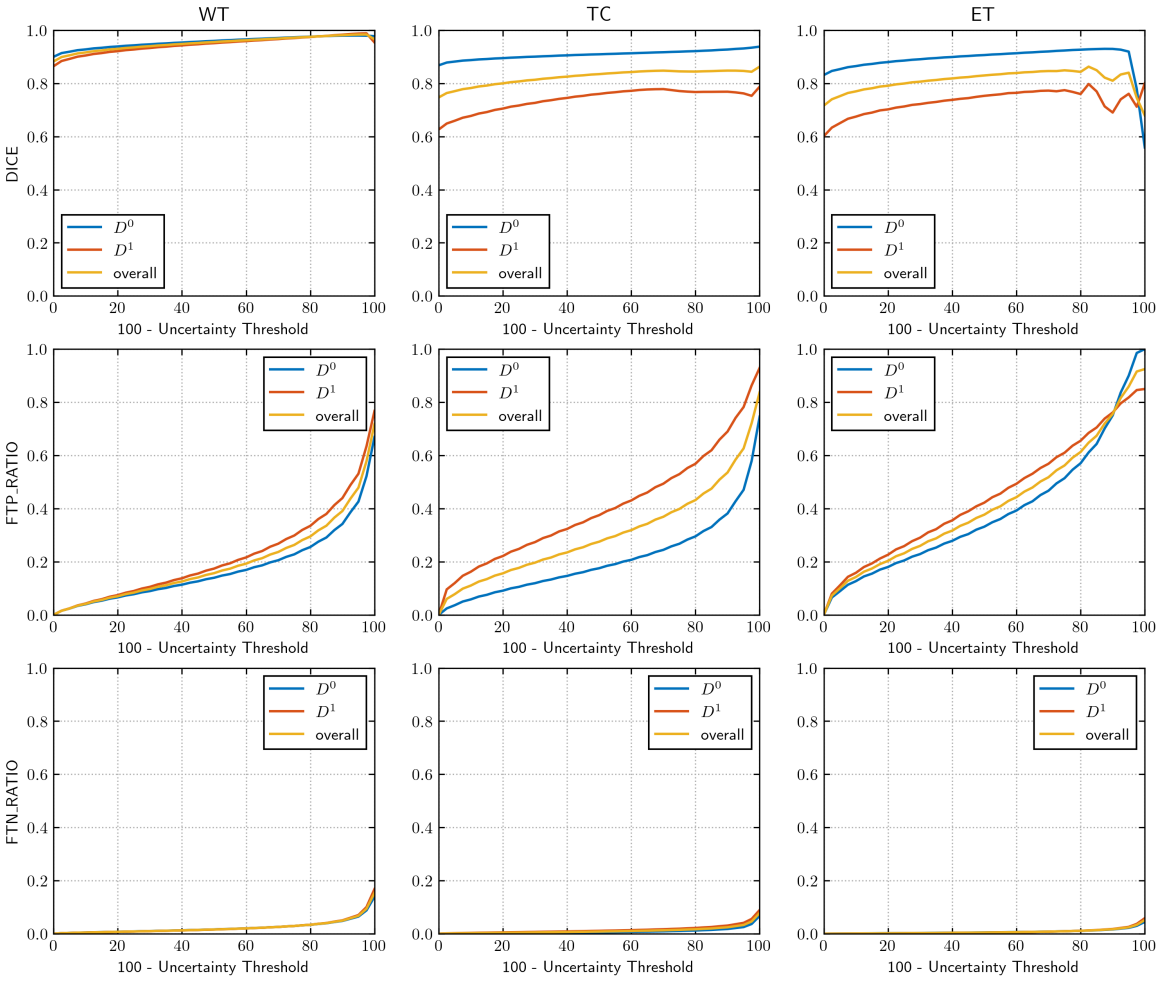

Figure 12: **BraTS:** We plot Dice, Filtered True Positive Ratio (FTP), and Filtered True Negative Ratio (FTN) as a function of uncertainty threshold for **GroupDRO-Model** on the BraTS dataset. Specifically, we plot Whole Tumour (WT), Tumour Core (TC), and Enhancing Tumour (ET) QU-BraTS (Mehta et al., 2022) metrics for both the D^0 and D^1 set.

B.1. Brain Tumour Segmentation - Experiment and Results for imaging centers based fairness and uncertainty evaluation

In this section, We use the 260 High-Grade Glioma (HGG) images from the publicly available Brain Tumour Segmentation (BraTS) 2019 challenge dataset. The image dataset is divided into two subsets based on the imaging center. Specifically, images coming from TCIA subset were considered in subgroup D^0, while images from the rest of the imaging center were considered in subgroup D^1. A Baseline-Model and a GroupDRO-Model are trained on a dataset of 74 samples from D^0 and 124 samples from D^1. While a Balanced-Model is trained on a balanced training set with 74 samples from each subgroup.

	Training Set		**Validation Set**	**Testing Set**	**BraTS Dataset**
	Baseline-Model and GroupDRO-Model	**Balanced Model**			
D^0	74	74	8	20	102
D^1	124	74	14	20	158
Overall	198	148	22	40	260

Table 27: Number of samples in both D^0 and D^1 subgroups for five different datasets: (i) Training Dataset used to train the **Baseline-Model** and the **GroupDRO-Model**, (ii) Training Dataset used to the train the **Balanced-Model**, (iii) Validation set for all three models, (iv) Testing set for all three models, and (v) for the whole BraTS dataset. We can observe that for the BraTS dataset, there is a high disparity between the number of samples for both subgroups.

Baseline-Model	**Dice**			**QU-BraTS Metric**		
	Whole Tumour	**Tumour Core**	**Enhancing Tumour**	**Whole Tumour**	**Tumour Core**	**Enhancing Tumour**
D^0	91.11	88.42	84.26	93.38	91.79	84.85
D^1	91.34	86.35	83.84	92.92	90.18	85.16
Fairness Gap	0.23	2.07	0.42	0.46	1.61	0.31

Table 28: Dice (at $\tau = 100$) and QU-BraTS metric (Mehta et al., 2022) values for Whole Tumour, Tumour Core, and Enhancing Tumour of a **Baseline-Model** on the BraTS dataset.

Balanced-Model	**Dice**			**QU-BraTS Metric**		
	Whole Tumour	**Tumour Core**	**Enhancing Tumour**	**Whole Tumour**	**Tumour Core**	**Enhancing Tumour**
D^0	90.49	88.28	83.73	92.96	91.18	86.16
D^1	91.23	83.78	81.79	92.95	89.08	85.64
Fairness Gap	0.74	4.50	1.94	0.01	2.10	0.52

Table 29: Dice (at $\tau = 100$) and QU-BraTS metric (Mehta et al., 2022) values for Whole Tumour, Tumour Core, and Enhancing Tumour of a **Balanced-Model** on the BraTS dataset.

GroupDRO-Model	Dice			QU-BraTS Metric		
	Whole Tumour	Tumour Core	Enhancing Tumour	Whole Tumour	Tumour Core	Enhancing Tumour
D^0	90.45	87.63	83.84	92.35	91.03	84.38
D^1	91.79	85.35	83.39	93.13	90.21	85.97
Fairness Gap	1.34	2.28	0.45	0.78	0.72	1.59

Table 30: Dice (at $\tau = 100$) and QU-BraTS metric (Mehta et al., 2022) values for Whole Tumour, Tumour Core, and Enhancing Tumour of a **GroupDRO-Model** on the BraTS dataset.

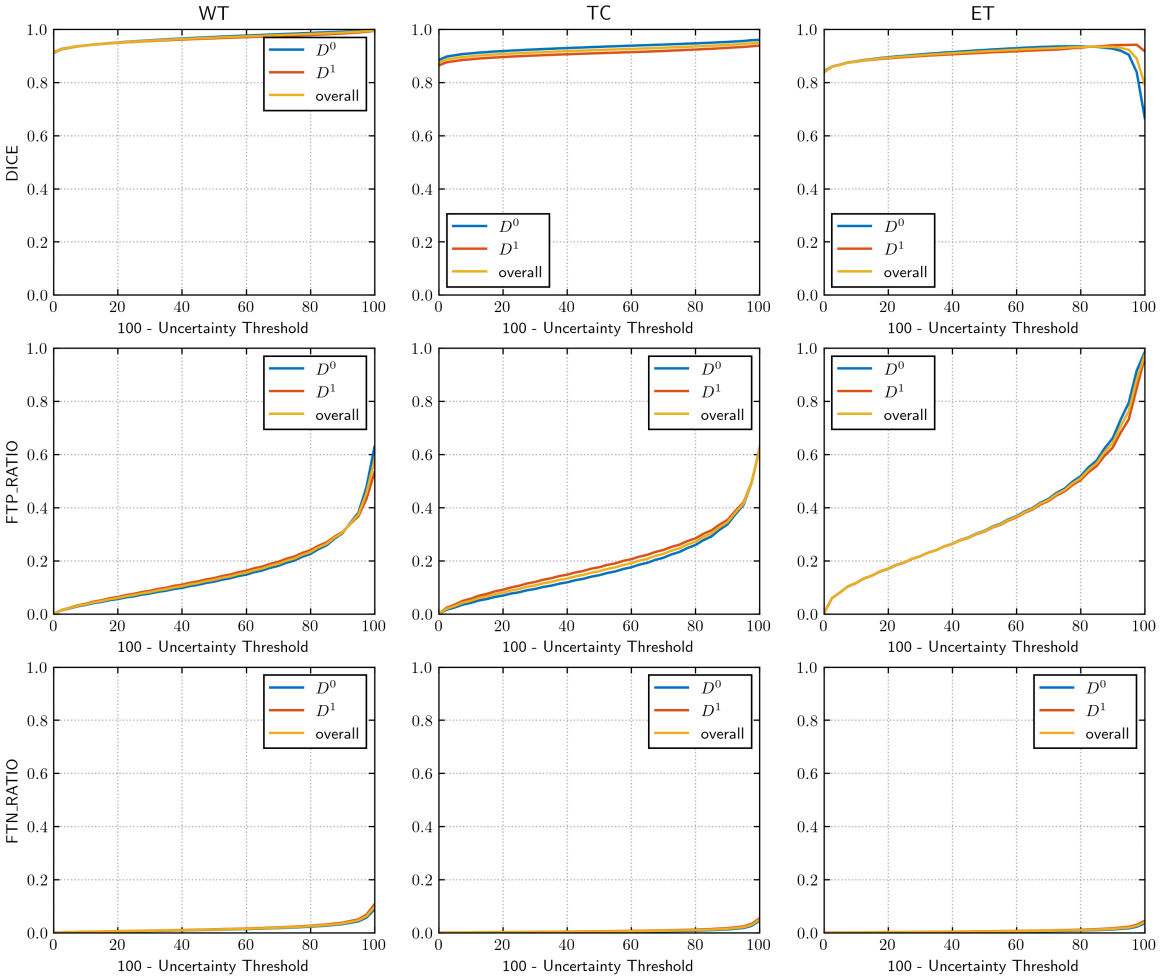

Figure 13: **BraTS-Imaging-Centre:** Dice, Filtered True Positive Ratio (FTP), and Filtered True Negative Ratio (FTN) as a function of uncertainty threshold for **Baseline-Model** on the BraTS dataset. Specifically, we plot Whole Tumour (WT), Tumour Core (TC), and Enhancing Tumour (ET) QU-BraTS (Mehta et al., 2022) metrics for both the D^0 and D^1 set.

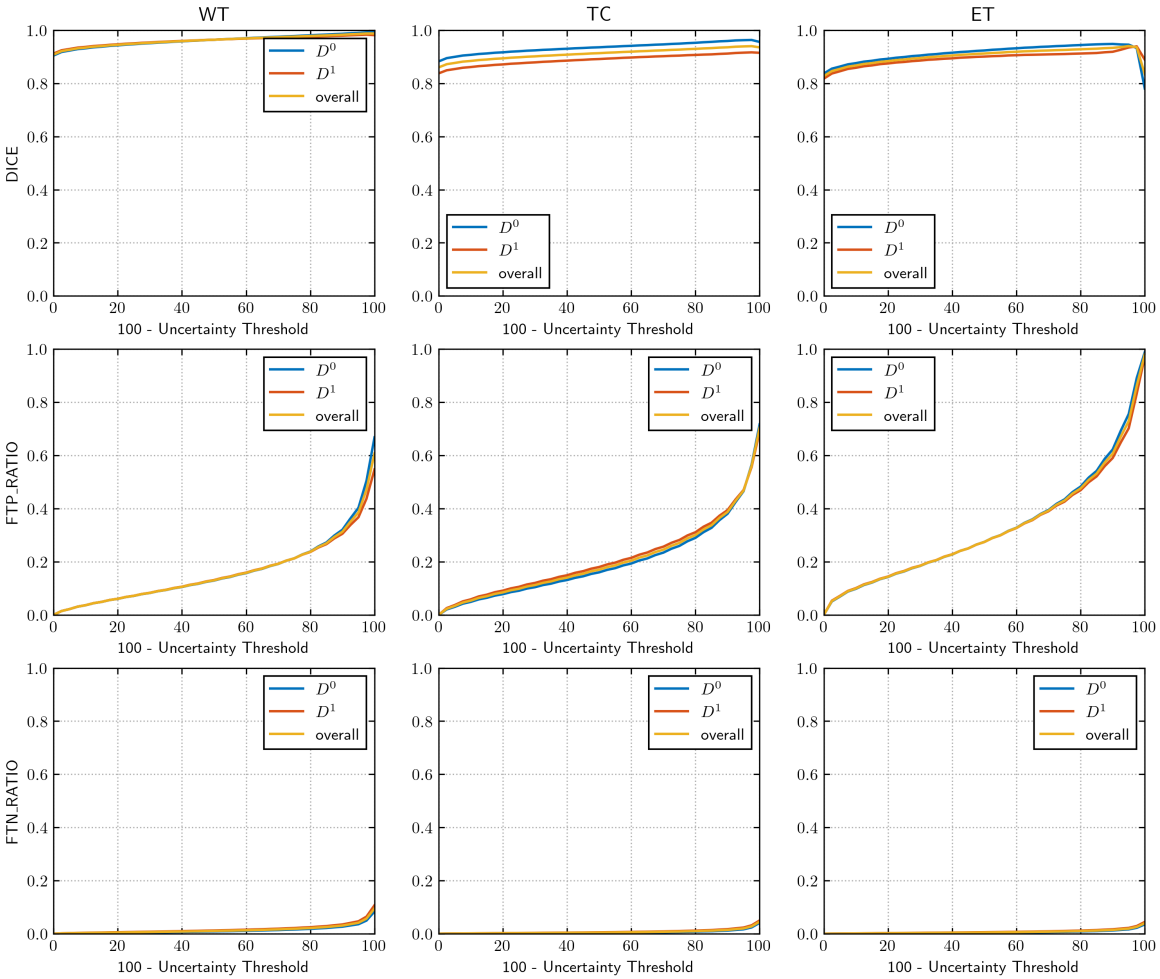

Figure 14: **BraTS-Imaging-Centre:** Dice, Filtered True Positive Ratio (FTP), and Filtered True Negative Ratio (FTN) as a function of uncertainty threshold for **Balanced-Model** on the BraTS dataset. Specifically, we plot Whole Tumour (WT), Tumour Core (TC), and Enhancing Tumour (ET) QU-BraTS (Mehta et al., 2022) metrics for both the D^0 and D^1 set.

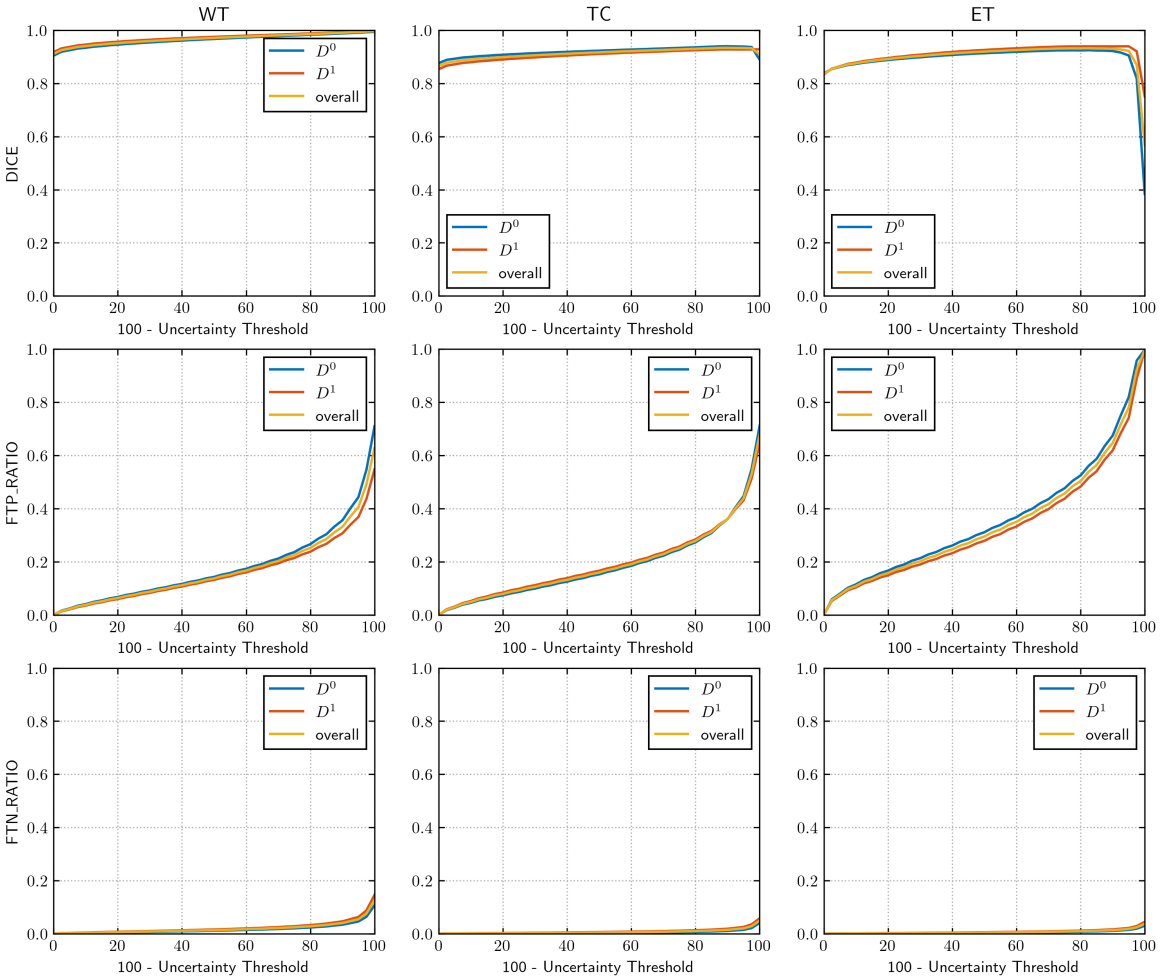

Figure 15: **BraTS-Imaging-Centre:** We plot Dice, Filtered True Positive Ratio (FTP), and Filtered True Negative Ratio (FTN) as a function of uncertainty threshold for **GroupDRO-Model** on the BraTS dataset. Specifically, we plot Whole Tumour (WT), Tumour Core (TC), and Enhancing Tumour (ET) QU-BraTS (Mehta et al., 2022) metrics for both the D^0 and D^1 set.

Appendix C. Alzheimer's Disease Clinical Score Regression

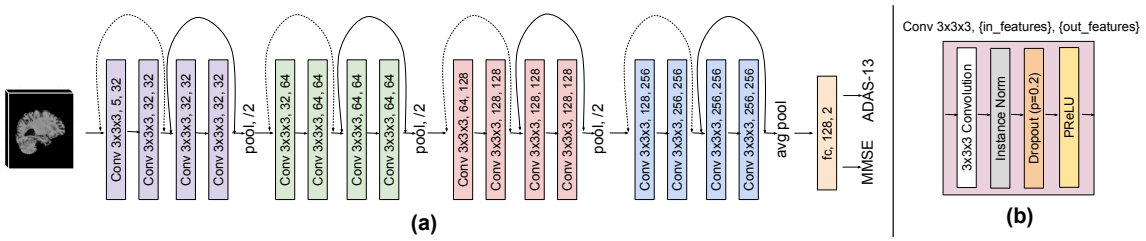

Figure 16: Network architecture diagram of modified 3D-ResNet-18 (Hara et al., 2018) for the Alzheimer's Disease clinical regression pipeline for predicting both ADAS-13 and MMSE scores. The network takes 3D T1-weighted MR image as input.

Implementation Details: A 3D ResNet34 (Hara et al., 2018) architecture was designed for the task of clinical score prediction [3]. The network was modified to be a multi-task network, such that it predicts both ADAS-13 and MMSE scores simultaneously. The network was trained to reduce the combined mean squared error losses for both ADAS-13 and MMSE. An Adam optimizer with a learning rate of 0.0002 and a weight decay of 0.00001 was used to train the network for a total of 200 epochs. The learning rate was decayed with a factor of 0.995 after each epoch. The code was written in PyTorch (Paszke et al., 2019) and ran on Nvidia GeForce RTX 3090 GPU with 24GB memory. For generating EnsembleDropout (Smith and Gal, 2018), we train three different networks with different random initialization of network weights and take 20 MC-Dropout samples (Gal and Ghahramani, 2016) from each. This results in a total of 60 Monte-Carlo samples for each image. As the total number of images is low in this dataset, we run the same experiments on five different folds and aggregate their results.

	ADNI Dataset			
	AD	**MCI**	**CN**	**Total**
D^0	33	187	39	259
D^1	112	311	183	606
Overall	145	498	222	865

Table 31: Number of images for each disease stage (AD, MCI, and CN) and each subgroup for the whole ADNI dataset. From this, we can see a high disparity between the total number of samples in each disease stage. Similarly, distribution across subgroups for a particular disease stage is also different.

3. https://github.com/kenshohara/3D-ResNets-PyTorch/blob/master/models/resnet.py

	Training Dataset (Baseline-Model and GroupDRO-Model)			
	AD	**MCI**	**CN**	**Total**
D^0	15	130	18	163
D^1	80	220	140	440
Overall	95	350	158	603

Table 32: Number of images for each disease stage (AD, MCI, and CN) and each subgroup for the training dataset used to train the **Baseline-Model** and the **GroupDRO-Model**. Similar to the whole ADNI dataset (Table-31), a high disparity between the total number of samples in each disease stage. Similarly, distribution across subgroups for a particular disease stage is also different.

	Training Dataset (Balanced-Model)			
	AD	**MCI**	**CN**	**Total**
D^0	15	130	18	163
D^1	15	130	18	163
Overall	30	260	36	326

Table 33: Number of images for each disease stage (AD, MCI, and CN) and each subgroup for the training dataset used to train the **Balanced-Model**. Compared to the training dataset used for the **Baseline-Model** and the **GroupDRO-Model** (Table-32), we balance the number of samples across both subgroups for each disease stage, but not across disease stages.

	Validation Dataset			
	AD	**MCI**	**CN**	**Total**
D^0	5	7	19	31
D^1	19	29	53	101
Overall	24	36	72	132

Table 34: Number of images for each disease stage (AD, MCI, and CN) and each subgroup in the Validation dataset for all three models (**Baseline-Model**,**GroupDRO-Model**, and **Balanced-Model)**. The distribution of samples across both subgroups and across different disease stages is similar to the Table-31.

	Testing Dataset			
	AD	**MCI**	**CN**	**Total**
D^0	13	14	38	65
D^1	13	14	38	65
Overall	26	28	76	130

Table 35: Number of images for each disease stage (AD, MCI, and CN) and each subgroup in the Testing dataset used to test all three models (**Baseline-Model**, **GroupDRO-Model**, and **Balanced-Model)**. The distribution of samples across both subgroups is kept similar, but it is not similar across different disease stages. We kept similar distribution across both subgroups for a fair comparison of their performance, while the distribution across different disease stages was not kept similar to reflect real-world scenarios where some disease stage can occur more frequently compared to others.

Baseline-Model	ADAS-13							
	RMSE				MAE			
	All	AD	MCI	CN	All	AD	MCI	CN
D^0	9.68	16.25	6.88	8.93	7.60	13.61	5.66	7.92
D^1	8.18	12.82	6.01	7.98	6.33	10.84	4.71	6.67
Fairness Gap	1.50	3.43	0.87	0.94	1.27	2.77	0.95	1.25

Table 36: Root Mean Squared Error - RMSE and Mean Absolute Error - MAE (at $\tau = 100$) for ADAS-13 score for All , Alzheimer's (AD), Mild-Cognitive Impairment (MCI), and Cognitive Normal (CN) samples of a **Baseline-Model** trained on the ADNI dataset.

Balanced-Model	ADAS-13							
	RMSE				MAE			
	All	AD	MCI	CN	All	AD	MCI	CN
D^0	10.57	17.25	7.13	10.20	8.54	14.86	6.01	9.54
D^1	8.84	13.49	6.86	8.33	6.94	11.44	5.31	7.34
Fairness Gap	1.73	3.76	0.26	1.87	1.59	3.42	0.70	2.19

Table 37: Root Mean Squared Error - RMSE and Mean Absolute Error - MAE (at $\tau = 100$) for ADAS-13 score for All , Alzheimer's (AD), Mild-Cognitive Impairment (MCI), and Cognitive Normal (CN) samples of a **Balanced-Model** trained on the ADNI dataset.

Balanced-Model	ADAS-13							
	RMSE				MAE			
	All	AD	MCI	CN	All	AD	MCI	CN
D^0	9.12	15.47	6.63	7.73	7.11	12.96	5.39	7.73
D^1	8.10	12.08	6.25	8.10	6.26	9.56	5.07	8.10
Fairness Gap	1.02	3.39	0.38	0.37	0.85	3.40	0.32	0.37

Table 38: Root Mean Squared Error - RMSE and Mean Absolute Error - MAE (at $\tau = 100$) for ADAS-13 score for All , Alzheimer's (AD), Mild-Cognitive Impairment (MCI), and Cognitive Normal (CN) samples of a **GroupDRO-Model** trained on the ADNI dataset.

Baseline-Model	MMSE							
	RMSE				MAE			
	All	AD	MCI	CN	All	AD	MCI	CN
D^0	2.37	4.43	1.57	1.69	1.79	3.89	1.26	1.52
D^1	2.21	3.45	1.72	2.00	1.75	2.86	1.40	1.72
Fairness Gap	0.16	0.99	0.15	0.31	0.03	1.03	0.14	0.20

Table 39: Root Mean Squared Error - RMSE and Mean Absolute Error - MAE (at $\tau = 100$) for MMSE score for All , Alzheimer's (AD), Mild-Cognitive Impairment (MCI), and Cognitive Normal (CN) samples of a **Baseline-Model** trained on the ADNI dataset.

Balanced-Model	MMSE							
	RMSE				MAE			
	All	AD	MCI	CN	All	AD	MCI	CN
D^0	2.57	4.10	1.87	2.44	2.11	3.56	1.58	2.44
D^1	2.41	3.14	1.96	2.73	2.00	2.52	1.64	2.48
Fairness Gap	0.16	0.96	0.09	0.29	0.12	1.04	0.06	0.04

Table 40: Root Mean Squared Error - RMSE and Mean Absolute Error - MAE (at $\tau = 100$) for MMSE score for All , Alzheimer's (AD), Mild-Cognitive Impairment (MCI), and Cognitive Normal (CN) samples of a **Balanced-Model** trained on the ADNI dataset.

GroupDRO-Model	MMSE							
	RMSE				MAE			
	All	AD	MCI	CN	All	AD	MCI	CN
D^0	2.19	3.88	1.68	1.52	1.63	3.07	1.33	1.34
D^1	2.23	3.09	1.91	2.15	1.73	2.43	1.51	1.73
Fairness Gap	0.05	0.79	0.23	0.63	0.10	0.64	0.18	0.39

Table 41: Root Mean Squared Error - RMSE and Mean Absolute Error - MAE (at $\tau = 100$) for MMSE score for All , Alzheimer's (AD), Mild-Cognitive Impairment (MCI), and Cognitive Normal (CN) samples of a **GroupDRO-Model** trained on the ADNI dataset.

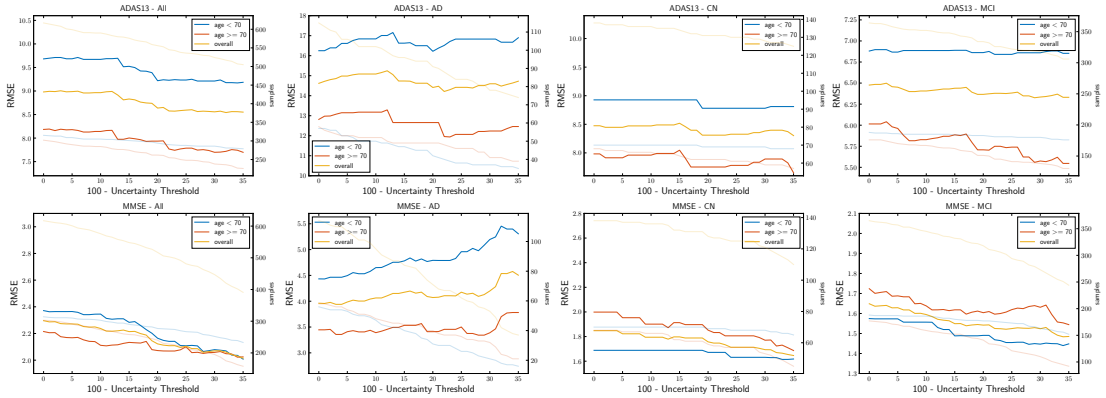

(a) Baseline Model

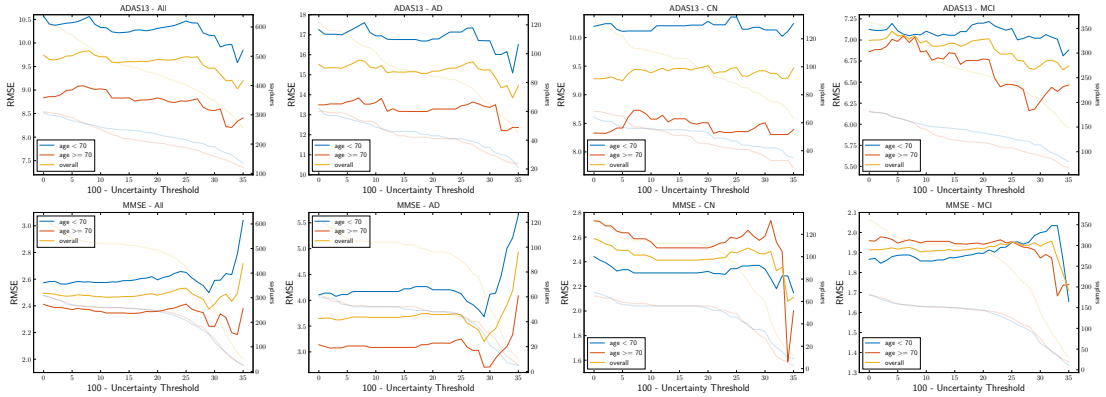

(b) Balanced Model

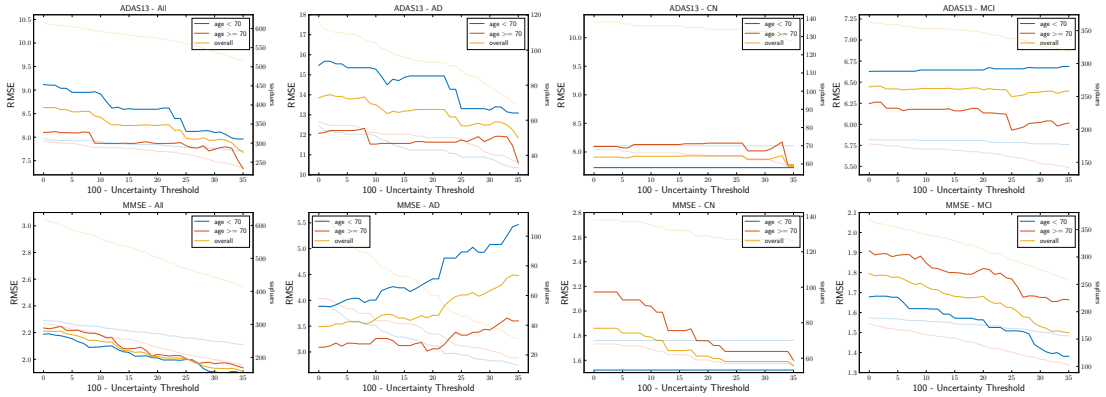

(c) GroupDRO Model

Figure 17: **ADNI:** Root Mean Squared Error (RMSE) of ADAS-13 (Top) and MMSE (Bottom) score prediction tasks as a function of uncertainty threshold for (a) **Baseline-Model**, (b) **Balanced-Model**, and (c) **GroupDRO-Model** on the ADNI dataset. Specifically, we plot RMSE for all samples as well as samples for each of the disease stages (AD, MCI, and CN) in each subgroup (D^0 - age < 70 and D^1 - age ≥ 70). The total number of samples as a function of uncertainty thresholds in are depicted with light colours in these plots.

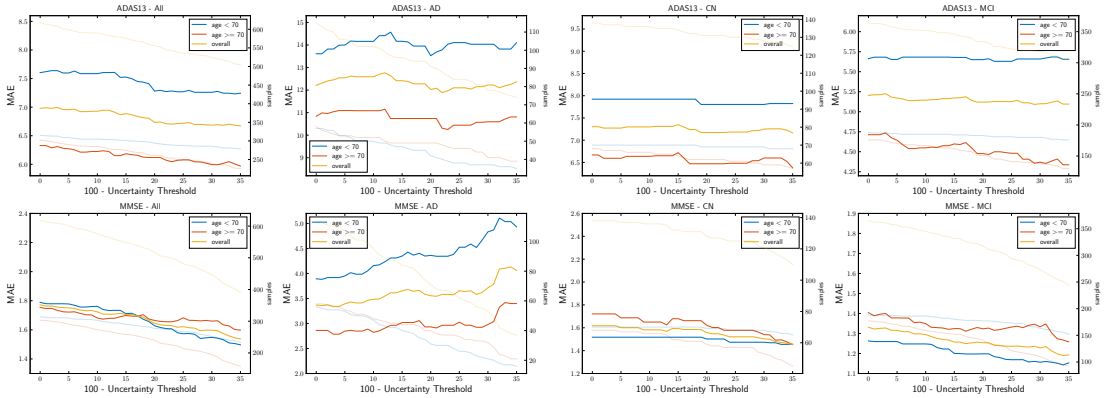

(a) Baseline Model

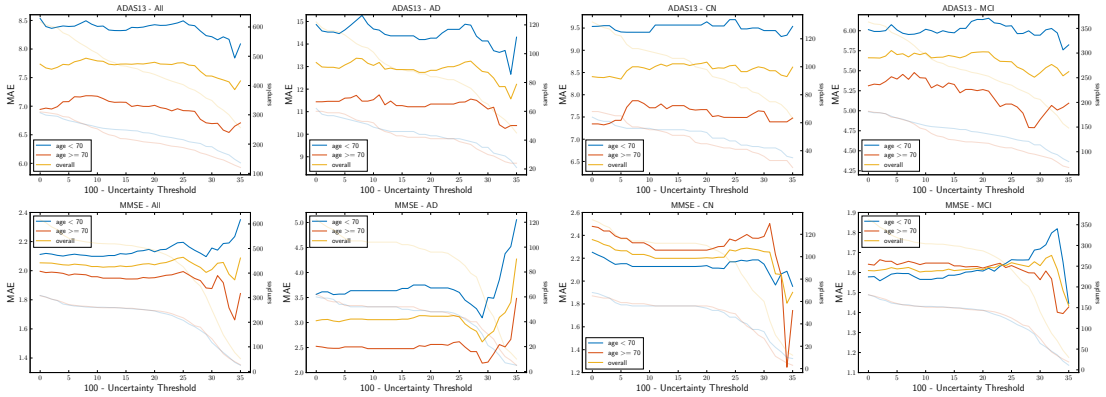

(b) Balanced Model

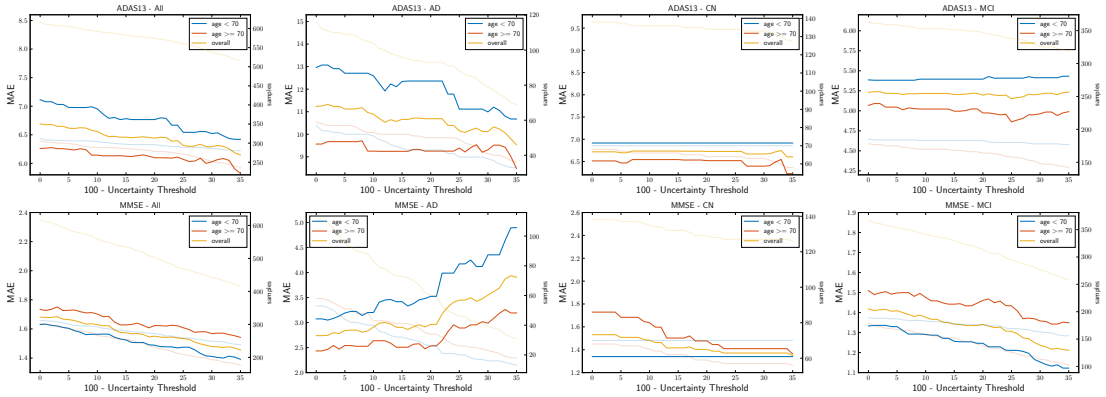

(c) GroupDRO Model

Figure 18: **ADNI:** Mean Absolute Error (MAE) of ADAS-13 (Top) and MMSE (Bottom) score prediction tasks as a function of uncertainty threshold for (a) **Baseline-Model**, (b) **Balanced-Model**, and (c) **GroupDRO-Model** on the ADNI dataset. Specifically, we plot RMSE for all samples as well as samples for each of the disease stages (AD, MCI, and CN) in each subgroup (D^0 - age < 70 and D^1 - age ≥ 70). The total number of samples as a function of uncertainty thresholds in are depicted with light colours in these plots.

Appendix D. Definition and Calculation of Uncertainty

Ensemble dropout (Smith and Gal, 2018): An ensemble of N networks is (ex. 3 independent networks) trained using the same dataset split but different network weight initialization. During test time, the same input is passed through this ensemble with dropout at test time to collect M different samples (ex. 20 samples) for each network. This results in a total of T=M*N sample (ex. 60 samples) outputs across these networks.

Entropy: It is a measure of the informativeness of the model's predictive density function for each model output $\hat{y}_i$. It is defined as:

$$\begin{aligned} H[\hat{y}_i|x_i] &= -\sum_{c=1}^{C} p(\hat{y}_i = c|x_i) \log \Big(p(\hat{y}_i = c|x_i) \Big) \\ &\approx -\sum_{c=1}^{C} \Big(\frac{1}{T} \sum_{t=1}^{T} p(\hat{y}_{i(t)} = c|x_i) \Big) \log \Big(\frac{1}{T} \sum_{t=1}^{T} p(\hat{y}_{i(t)} = c|x_i) \Big). \end{aligned} \tag{3}$$

where C is the total number of class labels, and $p(\hat{y}_{i(t)} = c|x_i)$ denotes output softmax probability for class c for sample t (Gal and Ghahramani, 2016; Lakshminarayanan et al., 2017; Smith and Gal, 2018). High entropy implies a flatter probability distribution across classes, while low entropy implies a more peaky probability distribution. Lower entropy shows that model is more confident in its prediction of the output class. Predictive entropy measures both epistemic and aleatoric uncertainties (which will be high whenever either epistemic is high or aleatoric is high) (Gal, 2016; Gal et al., 2017). Here we only consider entropy for the classification and the segmentation task. The calculation of entropy for a regression task requires calculating a normalized histogram, a computationally intensive process.

Sample Variance: The simplest uncertainty measure, sample variance, is estimated by computing the variance across the T samples collected Ensemble Dropout (Smith and Gal, 2018). For a regression task the variance in the output $\hat{y}_i$ for any input x_i, is defined as follows:

$$\mathrm{Var}(\hat{y}_i) = \frac{1}{T} \sum_{t=1}^{T} \hat{y}_{i(t)}^2 - \left(\frac{1}{T} \sum_{t=1}^{T} \hat{y}_{i(t)} \right)^2. \tag{4}$$

where $\hat{y}_{i(t)}$ is a prediction for sample t. Sample variance can be more simply interpreted as a measure of model output consistency across different samples.

Predicted Variance: For Predicted Variance, during training, in addition to the labels, the weights of the network are also trained to produce the prediction variance $\hat{V}$ at the output. Please refer to (Kendall and Gal, 2017; Nair et al., 2020) for more details about predicted variance.

Total Variance: Sample variance measures epistemic (model) uncertainty, while predicted variance measures aleatoric (data) uncertainty. The summation of both sample variance and predicted variance can give us the total variance (Gal, 2016; Kendall and Gal, 2017). We choose total variance for the regression task as it is computationally more feasible compared to the entropy for the regression task, and similar to the entropy, it also measures both aleatoric and epistemic uncertainties.